J. Fluid Mech. (2005), *vol.* 523, *pp.* 1–35. © 2005 Cambridge University Press
DOI: 10.1017/S0022112004000886 Printed in the United Kingdom

Migration of buoyant particles in low-Reynolds-number pressure-driven flows

By JAY T. NORMAN, HEBRI V. NAYAK AND ROGER T. BONNECAZE

Department of Chemical Engineering, The University of Texas at Austin, Austin, Texas 78712, USA

(Received 16 October 2003 and in revised form 24 May 2004)

Neutrally buoyant particles in low-Reynolds-number pressure-driven suspension flows migrate from regions of high to low shear, and this migration is a strong function of the local concentration. When the particle density differs from that of the suspending fluid, buoyancy forces also affect particle migration. It is the ratio between the buoyancy and viscous forces, as quantified by a dimensionless buoyancy number, which determines the phase distribution of the suspension once the flow is fully developed. Although several experiments have verified shear-induced particle migration in neutrally buoyant suspensions, data for particle migration when buoyancy effects are important are scarce. Electrical impedance tomography (EIT) is used here to non-invasively measure particle concentration across a pipe arising from the low-Reynolds-number flow of heavy conducting particles and light non-conducting particles in a viscous suspending fluid. A range of buoyancy numbers was investigated by varying the flow rate. In all of the experiments, a significant fraction of the particle phase was observed to migrate towards the top or bottom of the pipe, depending on the relative density of the particles. The amount of migration away from the centre of the pipe increased with increasing magnitude of the buoyancy number. Furthermore, observations of the phase distribution at several positions downstream of the inlet indicate that these suspension flows become fully developed earlier than that observed for neutrally buoyant particles. A scaling analysis for the prediction of the fully developed length is presented, which predicts shorter lengths for higher buoyancy numbers and is consistent with experimental observations. The experimental data were compared to an isotropic suspension balance model, and it was found that the particle phase distributions predicted by this model agree fairly well with the experimental observations.

1. Introduction

Particles in highly viscous suspension flows fall in the Stokes regime, where inertial effects are negligible. A unique property of these flows is the migration of particles away from areas of high shear. This phenomenon was first observed indirectly by Gadala-Maria & Acrivos (1980), where they noted a long-term decrease in the viscosity of a suspension in a Couette rheometer. They attributed this reduction in viscosity to the migration of particles to the low shear zone in the reservoir of the rheometer. Further studies by Leighton & Acrivos (1987) noted a short-term viscosity increase in the initial shearing of the Couette rheometer, which they attributed to the migration of particles across the gap of the rheometer. Furthermore, they demonstrated that this phenomenon was shear-induced particle migration, and they

used their studies to evaluate diffusion coefficients, which scaled as the shear rate and the square of the particle radius and was a strong function of concentration.

These studies prompted further investigations of shear-induced particle migration in other flow configurations. Several investigators have studied pressure-driven flows of neutrally buoyant particles in channels and pipes. Hampton *et al.* (1997) used nuclear magnetic resonance imaging (NMRI) to determine both velocity and concentration profiles of a pressure-driven pipe flow. They varied several experimental parameters including the bulk volume fraction ($0.10 \leqslant \phi_{bulk} \leqslant 0.50$) and the ratio of the radius of the particle a, to the radius of the pipe R ($a/R = 0.0256$ and $a/R = 0.0625$). For the largest a/R ratio with a bulk concentration of 10%, they observed no particle migration. However, larger concentrations showed significant particle migration to the centre of the pipe, with the profile becoming blunter with increasing concentration. Using laser-Doppler anemometry, Koh, Hookham & Leal (1994) measured the velocity and concentration profiles in pressure-driven channel flows of suspensions of neutrally buoyant particles. They observed particle migration for various concentrations ($\phi_{bulk} = 0.10, 0.20$ and 0.30) at several different ratios of particle radii to channel width. Their experiments revealed migration of the neutrally buoyant particles to the centre of the channel; however, some of their measurements may not have been at lengths sufficient to achieve a fully developed flow. Lyon & Leal (1997*a*, *b*) performed several experimental studies on neutrally buoyant particles in pressure-driven flows for longer channels. First, they studied the flow of a nearly monodisperse suspension of spheres using a modified laser-Doppler velocimetry (LDV) technique (1997*a*). They studied systems with the ratio of channel height to particle radius (H/a) of 11 to 24 and bulk volume fractions ranging from 0.30 to 0.50. These experiments revealed migration of particles to the centre of the channel, which increased with increasing bulk volume fraction. Lyon & Leal (1998*b*) also investigated a bidisperse suspension of neutrally buoyant particles with different radii using LDV. They found that the particles segregated with a greater fraction of large particles in the centre of the channel, and that this was more apparent at lower concentrations. Butler & Bonnecaze (1999) used electrical impedance tomography (EIT) to non-invasively image neutrally buoyant particles in a pressure-driven tube flow. They performed experiments with $a/R = 0.0064$ and for bulk concentrations of 0.25 and 0.40. These experiments revealed migration of the neutrally buoyant particles to the low-shear zones in the centre of the pipe. Furthermore, this non-invasive imaging technique produced results that closely matched the NMRI studies of Hampton *et al.* (1997).

Butler, Majors & Bonnecaze (1999) also performed NMRI studies of neutrally buoyant particles in oscillatory pressure-driven flow. They noted that these particles migrated to the centre of the pipe when the amplitude of oscillation was greater than the radius of the particle. However, when the amplitude was of the same order as the particle size, they observed particle migration to the walls.

Theoretical studies have focused around the development of two models: the diffusion flux model (Leighton & Acrivos 1987; Phillips *et al.* 1992) and the suspension balance model (Nott & Brady 1994). As the name implies, the diffusion flux model describes particle migration as a diffusive local process. The suspension balance model uses the equations of motion and appropriate constitutive equations to describe the suspension and particle phases.

Leighton & Acrivos (1987) introduced the diffusion flux model to successfully explain their observations of shear-induced particle migration in a Couette rheometer. This model describes the migration of particles with a diffusion equation, where the diffusion coefficient is proportional to the product of the shear rate and the square of

the particle radius ($D \sim \dot{\gamma} a^2$) and is a strong function of the particle concentration. This hydrodynamic diffusion arises due to the irreversible interaction among several smooth particles or two rough particles. Phillips *et al.* (1992) expanded this diffusion-flux model to pressure-driven flows. Based on the earlier studies of Leighton & Acrivos, they incorporated two mechanisms to explain particle migration. One accounts for particle concentration variation, where the rate of interactions of the particles is proportional to the shear rate and volume fraction. Therefore, an area of higher concentration will result in more hydrodynamic interactions, forcing the particle to areas of lower concentration. A second mechanism identifies gradients in the viscosity as a source of particle migration. When particles hydrodynamically collide in an area of non-uniform viscosity, the centre of mass of the two-particle system is changed, resulting in motion towards the lower viscosity (lower concentration). Phillips *et al.* successfully incorporated these mechanisms into a diffusion equation coupled (through the volume fraction dependency of the viscosity) with a momentum balance at low Reynolds number to model shear-induced particle migration in pressure-driven pipe flow.

One of the advantages of the diffusion flux model is its simplicity. Straightforward modifications of the equations of motion and the introduction of a diffusion equation are easily handled for many flows. This model has been applied with success to neutrally buoyant suspensions (for example see, Koh *et al.* 1994; Hampton *et al.* 1997; Subia *et al.* 1998; Butler & Bonnecaze 1999) and polydisperse (different radii) suspensions (Shauly, Wachs & Nir 1998). However, one disadvantage to this model is the local nature of the equations. There is a failure of the model at zero shear rate, resulting in a cusp with a value of maximum packing (for instance, the centreline in pressure-driven channel or tube flows). Furthermore, the diffusion flux model fails to predict particle migration accurately in curvilinear flows.

Jenkins & McTigue (1990) introduced a model for concentrated suspension flows for both the inertial and viscous regime. This model proposed that particle fluctuations play an important role in the transport of particles in a viscous flow. They introduced a model that describes the process in terms of the momentum due to the suspension phase and that occurring due to the fluctuations of the particles. They incorporated a suspension temperature and a balance equation for the energy to complete the model. Further, they introduced constitutive equations for the particle pressure, viscosity, heat flux and dissipation rate. Wallis (1969) had previously noted the importance of the additional pressure due to the particle phase in his description of one-dimensional two-phase flows.

Nott & Brady (1994) investigated neutrally buoyant particles in pressure-driven channel flow using Stokesian dynamics simulations. These simulations revealed that irreversible particle migration is present even without the mechanism of surface roughness. These Stokesian dynamics simulations revealed another important mechanism for particle migration: the variation in normal stresses. Nott & Brady used the insights from their simulations to introduce a macroscopic model similar to that proposed by Jenkins & McTigue to predict particle migration. This suspension balance model consists of volume-averaged continuity and equations of motion for the particle and suspension phases. Furthermore, constitutive equations are introduced for the stress of the suspension and particle phases. To eliminate the local description found in the diffusion flux model, Nott & Brady introduced the suspension temperature, which is a measure of the fluctuational velocities of the particles. They applied this model to a pressure-driven channel flow of monodisperse neutrally buoyant particles and found good agreement with the results of the Stokesian dynamics simulations.

Additionally, Nott & Brady (1994) have shown that the diffusion flux model can be obtained as a limiting case of the suspension balance model.

The suspension balance model has been successfully compared to several experimental studies. For instance, experiments of monodisperse neutrally buoyant suspensions in channel flow by Lyon & Leal (1998*a*) compared very favourably with the results predicted by the suspension balance model. Furthermore, Lyon & Leal (1998*b*) compared the results of their bidisperse (different radii) suspension experiments with the suspension balance model based on an average particle size and found reasonable agreement.

Nott & Brady (1994) expressed the stress attributed to the particle phase in terms of an isotropic particle pressure, the deviatoric shear stresses and a function of the normal stress differences. Their study focused on a rectilinear flow where the normal stress differences are not important. Morris & Boulay (1999) further investigated normal stress differences in curvilinear flows. Experimentally, little or no particle migration was observed in parallel-plate torsional flows; however, both models (the suspension balance model without normal stress differences or the diffusion flux model) predicted particle migration. Likewise, these models predicted no migration in cone-and-plate torsional flows, but experimental observations noted migration radially outward. To account for these phenomena in curvilinear flow, Morris & Boulay introduced a normal stress viscosity and a material tensor, which describes the anisotropy of the normal stresses, into the particle contribution to stress. This modification of the suspension balance model successfully captured the trends observed experimentally for parallel-plate torsional flows and cone-and-plate torsional flows. Fang *et al.* (2002) introduced a similar modification for the incorporation of normal stress differences in curvilinear flows. Furthermore, they successfully extended this formulation to the diffusion flux model by modifying the flux terms and the constitutive equation for the stress with a tensor that describes the anisotropy of the normal stresses.

In many suspensions, the density of the particles differs from that of the suspending fluid. To account for this additional effect, Morris & Brady (1998) incorporated buoyancy forces into the suspension balance model. This additional force is represented in terms of a buoyancy number, which is a measure of the ratio of the buoyancy forces to the viscous forces. For pressure-driven suspension flow in a pipe, this buoyancy number N_b may be expressed in terms of the average axial suspension velocity as

$$N_b = \frac{2(\rho_p - \rho_f) g R^2}{9\eta U}, \tag{1.1}$$

where ρ_p is the density of the particles, ρ_f is the density of the fluid, g is the acceleration due to gravity, R is the radius of the pipe, η is the viscosity and U is the average axial velocity.

Morris & Brady (1998) applied their modified suspension balance equations to pressure-driven channel flow and found good agreement with Stokesian dynamics simulations. They noted an increase in the deposition of the heavy particles for increasing buoyancy numbers, and they observed a dense fluid over light fluid for smaller-magnitude buoyancy numbers. Carpen & Brady (2002) have shown that this adverse density gradient is unstable for gravity-driven flows of non-neutrally buoyant particles. Furthermore, they found that as the density difference between the particles and the suspending fluid increases, the instability becomes more pronounced. However, they noted that the growth rate was small and a very long channel would be required to observe an adverse density gradient.

There are very few experimental data for low-Reynolds-number pressure-driven suspension flows with buoyant particles. One notable exception is a study performed by Altobelli, Givler & Fukushima (1991). They used NMRI to obtain both velocity and concentration profiles for systems of heavy particles at low Reynolds numbers. They studied systems with a particle volume fraction up to 39%. Although they were able to obtain excellent velocity profiles, the concentration profiles were only qualitative in nature, and they had difficulty resolving the concentration of particles near the surface of the pipe.

The purpose of this study is to make quantitative measurements of the concentration profiles of suspensions, where buoyancy forces are important. Here, the concentration profiles of heavy and light particles in pressure-driven pipe flow are determined using non-invasive EIT imaging. All of the experiments are performed at low pipe-Reynolds numbers, and vanishing particle-Reynolds numbers. In addition, the experimental results are compared to the local isotropic suspension balance model introduced by Nott & Brady (1994), hereinafter referred to as 'the model'.

The outline of the remainder of this paper is as follows. In § 2, EIT imaging is discussed. Specifically, the general theory of EIT measurements and image reconstruction is introduced. Then, in § 3, the experimental procedure, including the suspension preparation, fluid property measurements and experimental measurements are explained. In § 4, the model that is used for comparison to the experimental results is introduced. In § 5, measurements of the pressure along the pipe are presented. The pressure is observed to have a minimum before becoming fully developed, and a simple model is presented to explain this observation. In § 6, the measured migration for the suspensions is presented, along with a comparison to the theoretical predictions of the isotropic suspension balance model. In § 7, a scaling argument is presented to predict the length to obtain a fully developed concentration profile for pressure-driven flows of viscous suspensions with buoyant particles. Concluding remarks are presented in § 8.

2. Electrical impedance tomography imaging

EIT is a non-invasive imaging technique with many applications in the medical field and industrial processes (Cheney, Isaacson & Newell 1999; Dickin & Wang 1996). EIT has become a popular research and diagnostic tool for both medical and industrial applications because of the low cost of equipment and the non-invasive nature of this imaging procedure. For example, EIT has been used to successfully diagnose lung abnormalities, such as blood clots (Cheney *et al.* 1999). EIT has also been applied to several industrial applications. For example, Dickin & Wang (1996) successfully used EIT to monitor mixing tanks at a pilot plant scale. Additionally, Butler & Bonnecaze (1999) used EIT to determine concentration profiles of neutrally buoyant particles in a viscous pressure-driven pipe flow. Also, Etuke, Bonnecaze & Butler (1999) investigated the use of EIT in monitoring pulp consistency.

2.1. *EIT measurements*

EIT imaging is based on the variation in potential fields due to the applied current through a material with varying impedance. Figure 1 shows a common four-electrode measurement configuration for EIT imaging. A potential field, which is determined by the conductivity distribution in the imaging plane, is produced by introducing a current through a series of electrodes surrounding the plane of interest. The resulting potentials are measured at the electrodes surrounding the image plane. A

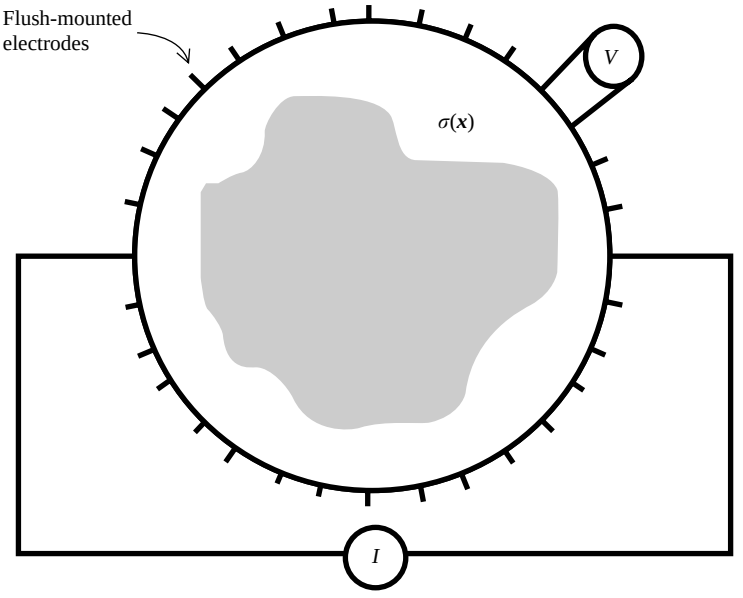

FIGURE 1. Four-electrode (opposite) measuring protocol. Current (I) is injected on flush-mounted opposing electrodes and the resulting potential differences (V) are measured on all adjacent electrodes not used for current injection. The current pair is shifted to the next pair of electrodes and potential measurements are obtained on the remaining electrodes. This procedure is repeated until all possible independent measurements are obtained.

nonlinear inverse algorithm is used to transform these potential measurements into the previously unknown conductivity field. Finally, the computed conductivity profiles are transformed to concentration fields of the multiphase flows using established correlations.

In this study, the Mark 2 (Mk.2) EIT data acquisition system (Etuke 1994) is used to perform all measurements. This system is a true impedance analyser in that it has the ability to perform electrical resistance tomography (ERT), electrical capacitance tomography (ECT) or electromagnetic tomography (EMT) measurements, with frequency ranging from 1 to 300 kHz. Other features of the Mk.2 include the ability to perform voltage or current injection and the choice of opposite or adjacent measurement protocols. As the name implies, current is injected through neighbouring electrodes in the adjacent protocol. In the opposite protocol, current is injected through opposing electrodes (figure 1). The resulting potential differences are measured on adjacent electrodes that are not used for current injection. This results in slightly more independent measurements for the adjacent protocol, but better quality measurements with the opposite protocol. This is because the current is more uniformly distributed in the opposite protocol, whereas the adjacent protocol produces a non-uniform current density that is larger in magnitude near the injection electrodes. Hence, the adjacent protocol is more sensitive to noise compared to the opposite protocol (Dickin & Wang 1996).

2.2. *Image reconstruction*

Conductivity profiles are obtained by numerically solving the nonlinear inverse problem, which is essentially the minimization of a square L_2 norm. The inverse problem is ill posed and results in an ill-conditioned matrix (Parker 1994). To address

these problems, a regularization technique is employed. A mathematical statement of the regularized inverse problem is given by

$$\min 2\chi(\boldsymbol{\sigma}) = \|\boldsymbol{W}_d \cdot (\boldsymbol{d}^{obs} - \boldsymbol{d}^{calc})\|_2^2 + \lambda \|\boldsymbol{W}_m \cdot (\boldsymbol{\sigma} - \boldsymbol{\sigma}_r)\|_2^2. \tag{2.1}$$

The first L_2 norm in (2.1) represents the minimization of the squared difference in the measured (noisy) data $\boldsymbol{d}^{obs}$ obtained from the Mk.2 system, and the calculated potentials $\boldsymbol{d}^{calc}$, which is determined with a pseudo-three-dimensional finite-element (FE) program (see Appendix A for further information). The data-weighting matrix $\boldsymbol{W}_d$ is a diagonal matrix consisting of the inverse of the squared potential measurements, which gives the lowest-magnitude potentials more weight since these measurements were found to be more accurate. The second L_2 norm represents the regularization of the inversion. Regularization ensures a sufficiently smooth solution of the conductivity $\boldsymbol{\sigma}$ relative to some reference conductivity $\boldsymbol{\sigma}_r$. In this study the model-weighting matrix $\boldsymbol{W}_m$ is either the identity matrix, which gives the solution that varies minimally from the reference conductivity, or the difference matrix (a simple representation of the first derivative), which results in the smoothest solution with respect to the reference conductivity. The parameter λ is a positive numerically determined coefficient, which is optimized in such a way as to prevent instability (the larger λ, the more heavily weighted is the second L_2 norm). Minimization of (2.1) results in an equation for the update in the conductivity profile. A numerical algorithm is implemented to determine the conductivity profile with the smallest L_2 error. The details of this procedure are outlined in Appendix B.

The inverse algorithm was verified by reconstructing synthetically produced potential measurements. The conductivity profile was chosen to be qualitatively representative of a system of heavy conducting particles. The corresponding synthetic potential measurements were obtained using the pseudo-three-dimensional forward FE simulation. Five per cent maximum Gaussian noise (average noise of 0.98%) and 10% maximum Gaussian noise (average noise of 1.94%) were added to the potential measurements. The maximum pointwise error for the conductivity in the reconstructed image was practically the same as the maximum Gaussian noise in both cases. Analysis of potential measurements for a uniformly conducting fluid indicates these measurements have an average error of 0.03% (Butler & Bonnecaze 1999). Further, the error in the reconstructed conductivity fields in the experiments was less than 5%. To further test the robustness and accuracy of the inverse procedure, several reconstructed experimental conductivity profiles were contaminated with 5% maximum random Gaussian noise. These noisy conductivity fields were used to generated synthetic potential measurements, which were inverted to produce new conductivity profiles. The absolute difference between the new and the original pointwise conductivities was also about 5% (see Norman 2004). These tests produced confidence in the robustness and accuracy of the inversion algorithm.

The forward problem is computed on a finite-element grid consisting of 2097 nodes and 1016 triangular elements (consisting of 6 nodes per element). With 32 electrodes, the maximum number of independent measurements for the opposite protocol is 448 (Butler & Bonnecaze 1999). However, the symmetry of this system reduces the maximum number to 224 independent measurements. Although the resolution increased with the number of elements used in the reconstruction algorithm, the computational time also increases with the number of elements. To address the balance of time and resolution, a maximum of 128 elements were used in the inverse problem. Each element represents a constant conductivity zone and, therefore, one independent

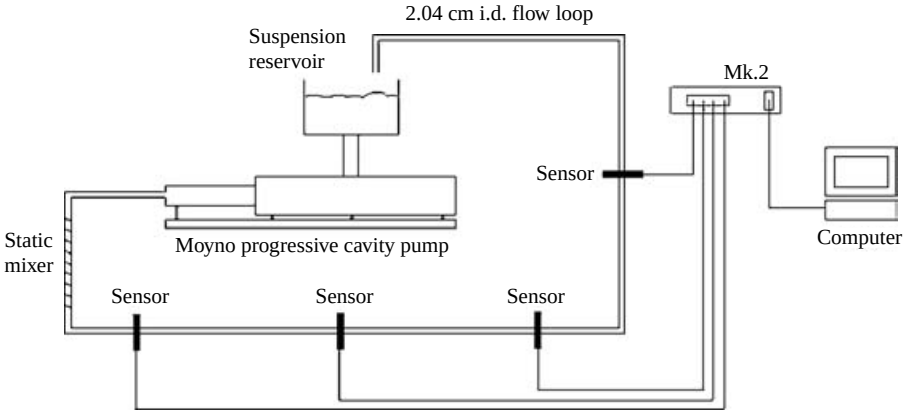

FIGURE 2. Schematic of the flow loop used for the experiments. A Moyno progressing cavity pump is used to create a pressure-driven flow through 2.04 cm i.d. pipe. A static mixer just downstream of the pump exit ensures an initially uniform distribution of the particles. Four sensors are shown, along with the Mk.2 system for measurement and a computer interface for data acquisition and manipulation. The total length of the flow loop is approximately 17 m.

measurement. All of the results in this paper are presented for a 32-electrode opposite-measurement protocol with 128 conductivity zones.

The inversion technique results in the unknown conductivity field, and the concentration profile is determined from one of the many well-known correlations relating particle concentration and the electrical properties of the fluid and particles. For the heavy conducting suspensions, the simplified Clausius–Mossotti correlation (Doyle 1977) was used to determine the concentration $\phi(\boldsymbol{x})$ profile, which is given by

$$\frac{\sigma(\boldsymbol{x})}{\sigma_s} = \left(\frac{2+2\phi(\boldsymbol{x})}{2-\phi(\boldsymbol{x})}\right)\left(\frac{2+\phi(\boldsymbol{x})}{2-2\phi(\boldsymbol{x})}\right), \tag{2.2}$$

where σ_s is the conductivity of the suspending fluid and $\boldsymbol{x}$ is a point in the domain. The non-conducting light particles required a slightly more complicated correlation to achieve the desired accuracy. A correlation developed by Meredith & Tobias (1961) was used for this conversion, where $\phi(\boldsymbol{x})$ is related to $\sigma(\boldsymbol{x})$ by

$$\phi(\boldsymbol{x}) = \frac{24 - [62 + 448(\sigma(\boldsymbol{x})/\sigma_s) + 64(\sigma(\boldsymbol{x})/\sigma_s)^2]^{1/2}}{2[8 + (\sigma(\boldsymbol{x})/\sigma_s)]}. \tag{2.3}$$

3. Experimental procedure

To measure buoyancy effects in low-Reynolds-number pressure-driven pipe flow, two different suspensions were pumped through the flow system illustrated in figure 2. The first suspension consisted of a highly viscous suspending fluid with heavy conducting spherical particles. Additionally, a second suspension consisting of light non-conducting particles was prepared and studied.

The flow system was equipped with three (light-particle suspension) or four (heavy-particle suspension) inline sensors consisting of 32 electrodes each. The electrodes were stainless steel, rectangular in shape and each have an area of 2 mm^2. After degassing to remove the entrained air, the suspension was poured into the reservoir, where it entered the Moyno progressing cavity pump. This pump was precisely controlled to ensure constant volumetric flow rates. The suspension was pumped through clear

Suspended particles	a (cm)	ρ_p (g cm^{-3})	ρ_f (g cm^{-3})	η (cP)	σ (S m^{-1})	ϕ
Conduct-O-Fil® S3000-S Heavy conducting	0.003	2.50	1.08	586	0.031	0.20
Extendosphere® SL-150 Light non-conducting	0.011	0.725	1.10	1055	0.164	0.25

TABLE 1. The average radii of the particles a, the density of the particles ρ_p, the density of the suspending fluid ρ_f, the viscosity of the suspending fluid η, the conductivity of the suspending fluid σ, and the volume fraction of particles in the suspension ϕ.

PVC pipes with an inner diameter of 2.04 cm. A static mixer was placed near the entrance to ensure an initially uniform distribution of the suspension. The sensor arrays were placed at predetermined lengths, to obtain measurements at different stages of progression towards fully developed flow. A pressure gauge was used to measure the pressure at several positions along the flow loop. The Mk.2 produced the current and measured the resulting potentials, which were stored and manipulated in a computer.

3.1. *Suspension preparation*

The suspending fluid consisted of UCON® lubricant 75-H-90000 to which an aqueous sodium iodide (NaI) solution was added to produce the desired viscosity, density and conductivity. An ERTCO hydrometer was used to measure the density, and a Cannon-Fenske viscometer was used to measure the viscosity. All of these measurements were conducted at room temperature and repeated numerous times to ensure accuracy. The particles were slowly added to the suspending fluid under vigorous stirring and then mixed for a minimum of twelve hours at a moderate speed. The suspension was then placed under vacuum to remove any entrained air. This was a long procedure, and since the particle density varied from that of the suspending fluid, separation of the phases always occurred. Therefore, to obtain an initially uniform distribution of particles, the suspensions were subsequently resuspended by mixing at very low speeds to ensure no air entrainment. Table 1 summarizes the composition and properties of each suspension.

The suspending fluid for the heavy particles consisted of 45% by volume of UCON® lubricant with an aqueous solution of 10 mg of NaI per cm^3 of distilled water. The conductivity of the suspending fluid was measured using Corning CheckMate 90 meter. The particles were silver-coated glass spheres (Conduct-O-Fil® S-3000S, by Potter's Industries) with a radius of approximately 0.003 cm. The suspending fluid for the light non-conducting particles was prepared as 50% by volume of UCON® lubricant with an aqueous solution of 25 mg of NaI per cm^3 of distilled water. These light particles were hollow spheres consisting mainly of Silica (Extendosphere®, SL-150, by PQ Corporation) and were sieved to give an average radius of 0.011 cm.

3.2. *Experimental conditions*

Table 2 summarizes the volumetric flow rate, Q, the measured pressure gradient determined from the last two pressure measurements, G_{exp}, the particle-Reynolds number, the pipe-Reynolds number, the buoyancy number $N_b = 2(\rho_p - \rho_f)gR^2/9\eta U$ and an alternative buoyancy number $\hat{N}_b = (\rho_p - \rho_f)g/G$ used for the numerical analysis (see § 6 for further information on the theoretical relationship between N_b

Experiment	Q ($cm^3\,s^{-1}$)	G_{exp} ($g\,cm^{-2}\,s^{-2}$)	$Re_{particle}$	Re_{pipe}	N_b	$\hat{N}_b$	$\hat{N}_b(G_{exp})$
Heavy							
1	37.1	1102	6.3×10^{-3}	2.12	4.9	1.3	1.3
2	18.9	674	3.2×10^{-3}	1.08	9.5	2.5	2.1
3	9.7	429	1.6×10^{-3}	0.55	18.6	4.4	3.3
Light							
4	10.8	1089	3.5×10^{-3}	0.35	−2.4	−0.5	−0.6
5	5.4	798	1.8×10^{-3}	0.18	−4.9	−1.0	−1.0
6	2.6	472	8.9×10^{-4}	0.09	−10.1	−1.9	−1.8

TABLE 2. Summary of the experimental conditions. Where the average volumetric flow rate is given by Q, the pressure gradient G_{exp} measured at the end of the pipeline, the particle-Reynolds number $Re_{particle}$, the pipe-Reynolds number Re_{pipe}, the buoyancy number given in terms of the average axial velocity (U) $N_b = 2(\rho_p - \rho_f)gR^2/9\eta U$ and buoyancy number given in terms of the pressure gradient, $\hat{N}_b = (\rho_p - \rho_f)g/G$.

and $\hat{N}_b$). Additionally, the buoyancy number $\hat{N}_b(G_{exp})$, which is expressed in terms of the pressure gradient given by G_{exp}, is displayed in table 2.

Three different volumetric flow rates were established for each suspension studied; these correspond to the buoyancy numbers presented in table 2, where N_b is the buoyancy number based on the average axial velocity, $\hat{N}_b$ is the buoyancy number used in the numerical analysis and $\hat{N}_b(G_{exp})$ is the buoyancy number based on the measured pressure gradient furthest downstream of the inline mixer. The buoyancy numbers $\hat{N}_b(G_{exp})$ and $\hat{N}_b$ are not necessarily equal because of discrepancies between theory and experiment, and the measured pressure gradient may not correspond to fully developed flow, as discussed in § 5. The volumetric flow rate was determined by averaging several measurements made with a graduated cylinder and a stopwatch and are displayed in table 2 along with the corresponding Reynolds numbers and the buoyancy numbers. The gauge pressure was measured at five points along the flow system for each experiment using an Ashcroft test gauge with increments of 0.1 p.s.i. The measured pressure and pressure gradients are discussed in detail in § 5.

3.3. *Data measurements*

The Mk.2 data acquisition system was used to obtain potential measurements at various predetermined lengths along the flow loop illustrated in figure 2. Although the Mk.2 has the ability to perform many measurement protocols, the current injection, 32-electrode opposite-protocol measurement technique (figure 1) produced the best reconstructed images (because the current is more uniformly distributed in the opposite protocol and therefore less sensitive to noise). Therefore, this measurement technique was used for all of the experiments. The sensor arrays were placed at four specific lengths for the heavy-particle suspension and three locations for the light-particle suspension. For the heavy particles, the first sensor was placed 5.5 m after the inline mixer. The remaining sensors were placed at 10.9 m, 12.4 m and 14.4 m after the inline mixer. The sensors for the light-particle suspension were placed at different positions, since fully developed flow is obtained at a shorter distance (see § 6 for further information on the fully developed length scale). These sensors were placed at 3.9 m, 5.3 m and 9.8 m after the static inline mixer. At each of these positions, the measurements were repeated a minimum of five times to ensure the precision of the

collected potential measurements. These potential measurements were averaged and manipulated as explained in Appendix C.

Once the Moyno pump was set to the desired volumetric flow rate, the suspensions were allowed to flow until a steady volumetric flow and pressure distribution were measured. Once the steady-state condition was established, the Mk.2 system was attached to each sensor via 32 gold-plated connectors. The electrodes were connected to the Mk.2 in such a way that ensures the position of the first measurement was known, which was important since the inverse algorithm requires the first electrode position to be defined. The frequency was set at 2 kHz for every measurement and a typical current of 1 mA was injected across opposing electrodes. The electrophoretic velocity produced by this current was three orders of magnitude less than the corrected Stokes velocity. The 32-electrode opposite-protocol measurement technique resulted in 448 measurements (not all of which are independent), which were obtained within 5 s at 2 kHz. Every measurement was repeated a minimum of five times to ensure precision and the average values were used in the numerical analysis.

4. Suspension balance model

As discussed in § 1, theoretical studies on low-Reynolds-number particle migration have focused around the development of two models: the diffusion flux model and the suspension balance model. The suspension balance model has been successfully applied to several suspension flows, including pressure-driven channel flow with buoyancy effects. For this reason, the suspension balance model is used for comparison to experimental results. Furthermore, the model introduced by Nott & Brady (1994) is investigated in this study. The suspension balance model consists of the averaged equations of motion for the suspension and particle phases and appropriate constitutive equations.

4.1. *Isotropic suspension balance model*

In this study, a fully developed steady-state flow that includes the in-plane velocities is considered. The non-dimensional suspension-phase equations are given by

$$\nabla \cdot \langle \boldsymbol{u} \rangle = 0, \tag{4.1a}$$

$$-\nabla P - \nabla \Pi + 2\nabla \cdot \eta_s \langle \boldsymbol{e} \rangle + \hat{N}_b \phi \boldsymbol{e}_y = 0. \tag{4.1b}$$

Here, ϕ is the volume fraction of particles, η_s is the suspension viscosity given by (4.1d). The parameter Π is the particle pressure (given in (4.1c)) and P is the fluid pressure, which are non-dimensionalized by GR, where G is the axial pressure gradient and R is the radius of the pipe. Further, $\boldsymbol{u}$ is the velocity of the suspension phase, which is non-dimensionalized by GR^2/η, where η is the viscosity of the suspending fluid. All lengths are scaled by the radius of the pipe R, and the buoyancy number is $\hat{N}_b = (\rho_p - \rho_f)g/G$. The volume-averaged bulk rate-of-strain tensor is denoted by $\langle \boldsymbol{e} \rangle$. Note that it is easier to solve this multiphase flow for fixed $\hat{N}_b$ rather than for fixed N_b because the latter requires an iterative solution to determine the pressure gradient that corresponds to the desired averaged velocity. Therefore, N_b is computed as a function of $\hat{N}_b$ (figure 11) and used to map the experimental conditions (fixed N_b) into the equivalent numerical condition (fixed $\hat{N}_b$).

Experimental studies by Zarraga, Hill & Leighton (1999) suggest the particle pressure is best represented by the correlation

$$\Pi = 1.89\phi^3 \left(1 - \frac{\phi}{\phi_m}\right)^{-3} \dot{\gamma}, \tag{4.1c}$$

where $\dot{\gamma} = [\langle \boldsymbol{e} \rangle : \langle \boldsymbol{e} \rangle]^{1/2}$ is the shear rate, which is non-dimensionalized by GR/η. Further, they correlated the suspensions viscosity as

$$\eta_s = \mathrm{e}^{-2.34\phi} \left(1 - \frac{\phi}{\phi_m}\right)^{-3}. \tag{4.1d}$$

Sierou & Brady (2002) have found that these expressions for the particle constitutive equations are in good quantitative agreement with the predictions of Stokesian dynamics simulations.

The non-dimensional particle-phase equations are given by

$$\nabla \cdot \phi \langle \boldsymbol{u} \rangle_p = 0, \tag{4.2a}$$

$$-\nabla \Pi - \frac{9\phi}{2f(\phi)} \left(\frac{R}{a}\right)^2 (\langle \boldsymbol{u} \rangle_p - \langle \boldsymbol{u} \rangle) + 2\nabla \cdot \eta_p \langle \boldsymbol{e} \rangle + \hat{N}_b \phi \boldsymbol{e}_y = 0. \tag{4.2b}$$

Here, $f(\phi) = (1-\phi)(1-\phi/\phi_m)^{1.82}$ is the hindrance function (it should be noted that other hindered settling functions, such as the Richardson–Zaki correlations were used; however, owing to the small ratio of particle to pipe radius and the resulting no-slip between phases, the form of the correlation had little or no effect in the numerical analysis), R is the radius of the pipe and a is the radius of the particle. These equations were non-dimensionalized using the same characteristic quantities used for the suspension phase.

This form of the local isotropic suspension balance equations allows the phase slip (i.e. $w_p - w$) to be explicitly calculated, which was found to be practically zero. Furthermore, the velocity components are allowed to vary in the plane of interest, allowing for recirculation. Additionally, the volume fraction of particles is constrained such that the integral of the concentration profile over the domain is equal to the bulk volume fraction. In these experiments, the measured parameters are the suspension flow rate at the exit of the flow loop and the areal averaged particle concentrations obtained from integrating the concentration profiles obtained from the EIT. Therefore, these constraints are used in the numerical model. In fact, the axial flux or mixing cup average volume fraction at the inlet is not measured, which in a closed flow loop will be different from the initial mixture in the tank once steady state has been achieved.

4.2. *Numerical analysis*

These equations are solved simultaneously, using a least-squares finite-element method (LSFEM) numerical algorithm (Nayak 2001; Nayak & Carey 2003). The standard LSFEM is based on constructing a global error functional involving the square L_2 norm of the residuals of the differential equations governing the flow. The objective is to determine the dependent variables such that the global error functional is minimized. When the field or dependent variables satisfy the differential equations, the local and the global residuals and, hence, the global error functional are minimized. The local and global residuals also provide an indication as to how well the individual governing equations have been satisfied over each element of the FE domain and over the whole computational domain. The application of the least-squares approach results in strongly coupled nonlinear algebraic equations for the nodal variables. This system of equations is solved iteratively. Furthermore, this nonlinear minimization problem is solved by incorporating a line search with the classical Newtonian method at each iteration step, and this procedure does not require the use of preconditioners.

The principal objective of any nonlinear iteration method is to reduce the discrete residuals to a value of zero (within the machine tolerance). In all of the simulations,

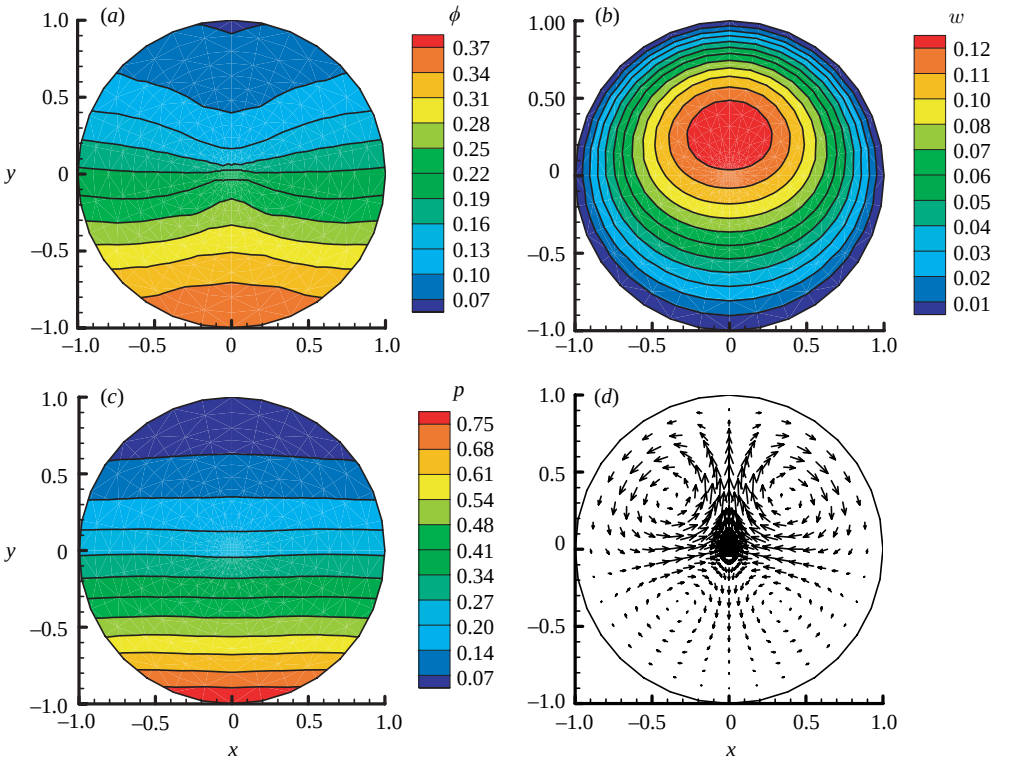

FIGURE 3. Numerical solution of the isotropic suspension balance equations. These results represent a suspension of heavy-particles with the properties represented in table 2 for a buoyancy number (according to (1.1)) of 9.5. (*a*) Volume fraction distribution; (*b*) non-dimensional axial velocity distribution; (*c*) non-dimensional pressure distribution; (*d*) vector representation of the in-plane velocity distribution.

Newton's iteration is assumed to be converged when the global error functional is less than or equal to the tolerance value of 10^{-4}. Computations of these suspension-flow equations confirm that this tolerance limit is adequate in order to obtain high-quality numerical solutions. A more formal mathematical treatment and detailed discussion about LSFEM are given in Nayak (2001) and Nayak & Carey (2003). For this analysis, the computational domain is a circle with a non-dimensional radius of one. This mesh is composed of 128 p-version 9-noded quadrilateral elements. Furthermore, the no-slip condition is imposed on the boundary of the domain. For both negative and positive buoyancy numbers, the numerical simulations have been performed over a wide range of buoyancy numbers in small increments. In all computations, the solutions for a higher flow rate and, hence, a lower buoyancy number, is used as the initial guess for the flow simulation at the next higher buoyancy number. The solution for the neutrally buoyant flow case was used as the initial guess for the first non-zero buoyancy number.

4.3. *Numerical results*

Figure 3 is a typical example of the results obtained from the numerical analysis of the suspension balance equations, which were performed at the intermediate buoyancy number ($N_b = 9.5$) for the heavy-particle suspension. Figure 3(*a*) depicts the particle concentration profile and figure 3(*b*) represents the axial velocity distribution for a

fully developed steady-state flow. Furthermore, figure 3(*c*) is the pressure distribution and figure 3(*d*) is a vector plot of the in-plane velocities; it is important to note that the in-plane velocities are two orders of magnitude smaller than the axial velocity.

As seen in figure 3(*a*), buoyancy forces strongly affect the distribution of the particles, with the heavy particles accumulating at the bottom of the pipe. Figure 3(*b*) depicts the axial velocity profile for this system and reveals the effect of particle deposition on the velocity distribution. The maximum velocity occurs above the centre of pipe because of the higher concentration of particles and hence greater viscosity at the bottom. Figure 3(*c*) shows the pressure distribution for this system, revealing that the pressure varies in the cross-sectional plane and indicates that this parameter should be included in the numerical analysis. Figure 3(*d*) is a vector representation of the in-plane velocities. This figure shows a clear recirculation pattern similar to that found by Zhang & Acrivos (1994). Furthermore, this recirculation results in a qualitative and quantitative change in the concentration distribution. Specifically, the recirculation affects the resuspension of the particles and it results in a concentration profile that exhibits curvature, such as that seen in figure 3(*a*). When the in-plane velocities are assumed to be zero and are not included in the numerical simulation, the resulting concentration profiles show almost no dependency in the horizontal direction.

5. Pressure measurements

Measurements of the pressure along the pipe give important insight into the development of the suspension flow and may be used as an indicator of fully developed flow. Figure 4 shows the gauge pressure ($\mathrm{g\,cm^{-1}\,s^{-2}}$) at various positions in the flow loop downstream of the inline mixer. The pressure gradient is obtained from the data presented in figure 4 using second-order finite differencing.

The pressure gradient decreases from the initially well-mixed suspension to a minimum that occurs approximately halfway through the pipeline (figure 5). After this point, the pressure begins to increase. For the heavy particles (figure 5*a*), the pressure gradient continues to increase to the end of the pipeline. For the light particles, figure 5(*b*) suggests an approach towards plateaux in the pressure gradients, which would indicate a fully developed flow has been established.

The development of the pressure gradient can be understood by considering a simple problem. Consider a pressure-driven flow between two flat plates, separated by a distance H, as illustrated in figure 6.

This channel flow has been separated into two zones. The upper zone with a height of αH represents a section of the flow that has a lower concentration of particles ϕ_1, than the lower zone of the flow with a concentration of ϕ_2. The average concentration of particles in the suspension, ϕ_b, is assumed to be fixed and is given by

$$\phi_1\alpha + \phi_2(1-\alpha) = \phi_b, \tag{5.1}$$

The flow is a simple pressure-driven channel flow and the momentum equations are

$$\frac{\partial}{\partial y}\left[\eta_1(\phi_1)\frac{\partial V_1}{\partial y}\right] = -G, \tag{5.2a}$$

$$\frac{\partial}{\partial y}\left[\eta_2(\phi_2)\frac{\partial V_2}{\partial y}\right] = -G, \tag{5.2b}$$

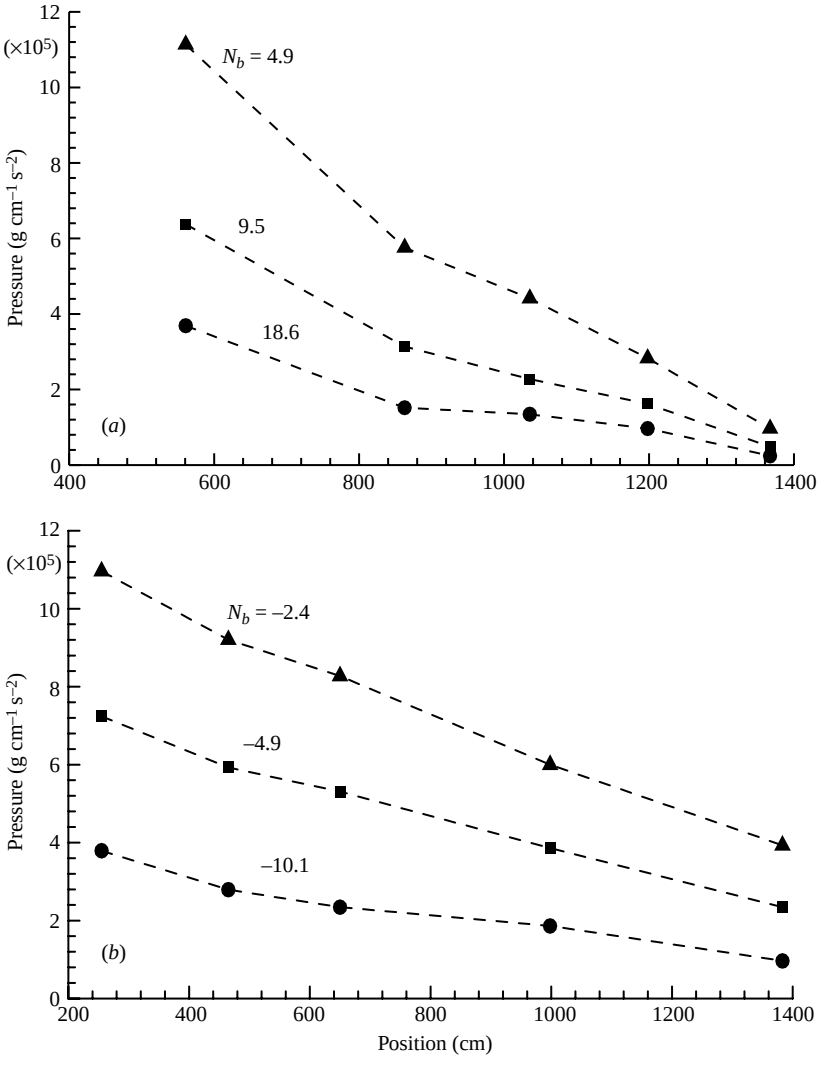

FIGURE 4. Pressure measurements downstream of the static inline mixer. (*a*) Pressure for the heavy, silver particle suspension; (*b*) pressure for the light, PMMA particle suspension.

where V_1 is the velocity in the upper zone, V_2 is the velocity in the lower zone and y is the vertical direction. Additionally, ϕ_1 is the volume fraction of particle in the upper zone with a viscosity $\eta_1(\phi_1)$, and ϕ_2 is the volume fraction in the lower zone with a viscosity of $\eta_2(\phi_2)$. Applying the usual no-slip conditions and continuity of the stress boundary conditions, the pressure gradient is related to the average flow rate by

$$\frac{G}{G_{wm}} = \frac{\eta_1\eta_2 H^3}{2\eta_b(\eta_2 A + \eta_1 B)}, \tag{5.3a}$$

where

$$A = \frac{3}{2}\left\{\frac{H[(2\alpha-\alpha^2)+\beta-\beta(2\alpha-\alpha^2)]}{\alpha+\beta(1-\alpha)}\right\}(H-\alpha H)^2-(H-\alpha H)^3, \tag{5.3b}$$

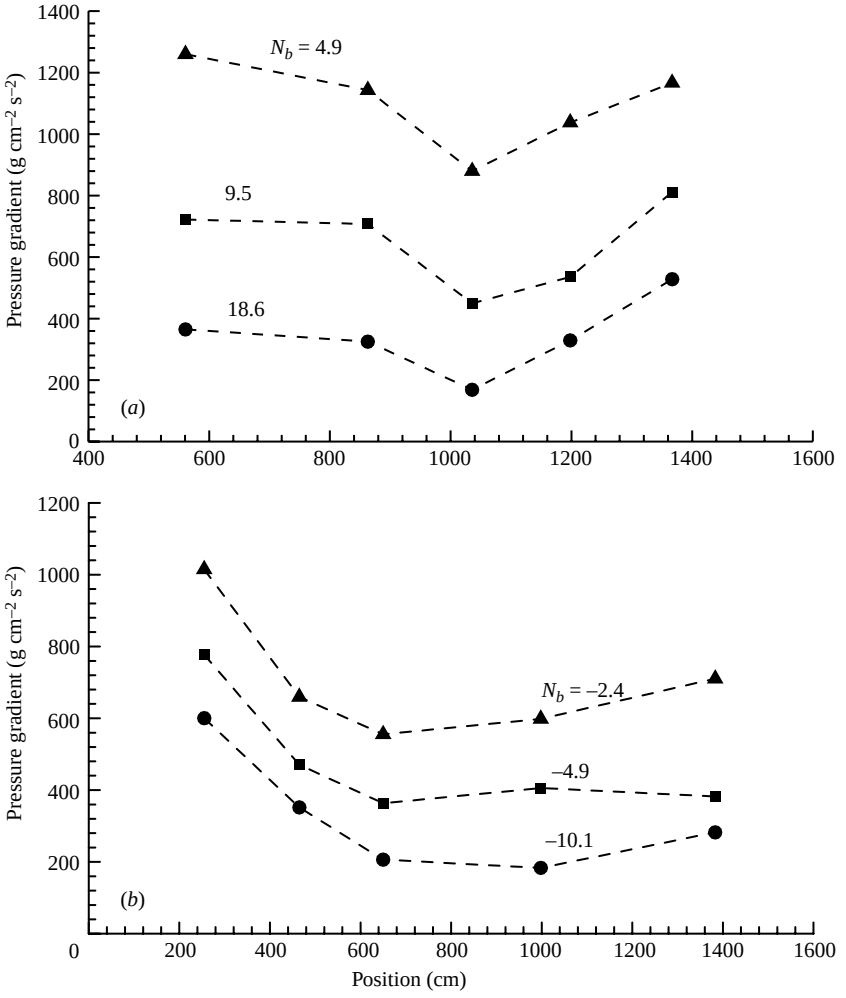

FIGURE 5. Pressure gradient measurements downstream of the static inline mixer. (*a*) The pressure gradient for the heavy, silver particle suspension; (*b*) the pressure gradient for the light, PMMA particle suspension.

$$B = (H-\alpha H)^3 - H^3 + 3\alpha H^3 + \frac{2\alpha-\alpha^2+\beta+\beta(2\alpha-\alpha^2)}{\alpha+\beta(1-\alpha)}\left\{\frac{3H(H^2-(H-\alpha H)^2)}{2} - 9\alpha^3 H^3\right\}. \quad (5.3c)$$

Here, $\beta = \eta_1/\eta_2$ and $G = -\partial P/\partial x$, and the viscosity is volume-fraction dependent and given by $\eta_i = 1/[1-(\phi_i/\phi_{max})]^2$, where $\phi_{max} = 0.63$. Also, G_{wm} is the pressure gradient for a well-mixed suspension of particles with a bulk volume fraction of ϕ_b.

It is instructive to view the pressure gradient as a function of the fractional size of the top layer. Figure 7 presents data for the pressure gradient normalized by the pressure gradient for a well-mixed suspension of equivalent properties.

This figure reveals that the pressure gradient required to maintain a constant volumetric flow rate is lower for smaller heights and lower concentration of particles in this area. For a flowing suspension of heavy particles, this implies that the pressure gradient should initially drop and then will eventually rise to a new plateau value.

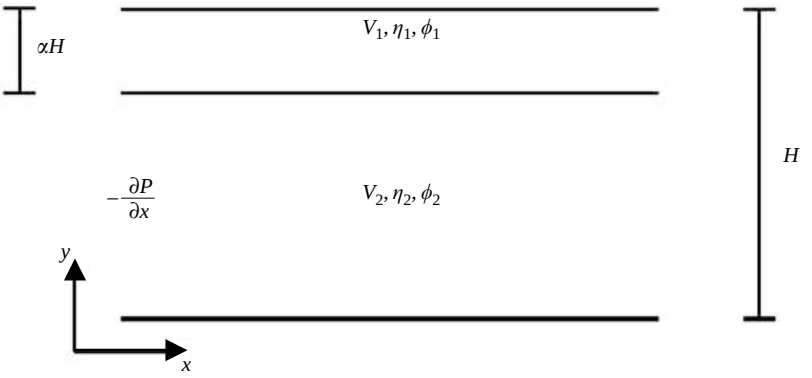

FIGURE 6. Schematic of a fully developed unidirectional pressure-driven flow. The channel has a height, H, where the upper section (αH) contains a suspension of viscosity $\eta_1(\phi_1)$, and the lower section ($H-\alpha H$) contains another suspension of viscosity $\eta_2(\phi_2)$.

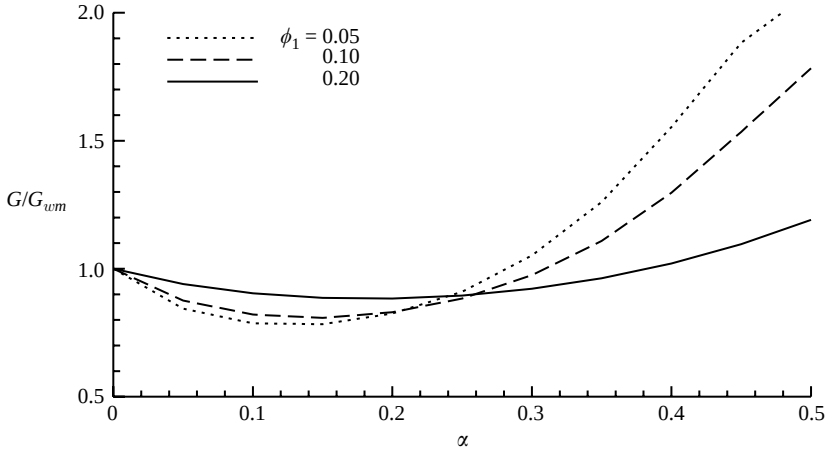

FIGURE 7. Pressure gradient (normalized by the pressure gradient for a well-mixed suspension) required to maintain a constant volumetric flow rate as the height (αH) of the top section increases. Data for particle volume fraction of 0.05, 0.10 and 0.20 in the top section, with a bulk volume fraction of 0.30.

Figure 8 is a comparison of the pressure gradients measured furthest downstream and the theoretical pressure gradient predicted from the isotropic suspension balance model. The experimental and theoretical pressure gradients for the light-particle suspension match quite well. The experimentally observed pressure gradient for the heavy-particle suspension is generally larger than the theoretical prediction. A small change in the distribution of the particles may have significant impact on the pressure gradient, which could account for the discrepancy in figure 8 between theory and experiment for the suspensions of heavy particles.

6. Results

The results for the experiments discussed in § 3 are presented in this section. All of the experiments were modelled using the local isotropic suspension balance equations presented in § 4, and these are compared to the experimental observations.

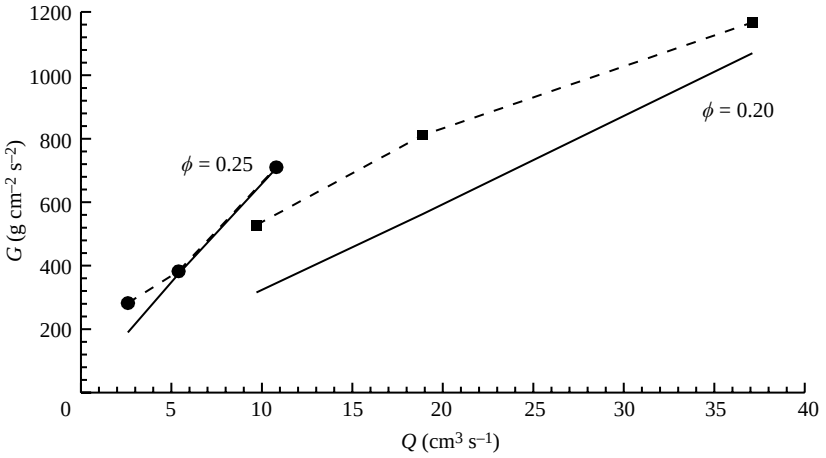

FIGURE 8. Comparison of the experimental fully developed pressure gradients (G) and the predictions of the isotropic suspension balance model at equivalent volumetric flow rates (Q). The circular symbols represent the light-particle experimental data and the square symbols represent the heavy-particle suspension. The solid lines indicate the theoretical predictions.

Additionally, our experimental results are compared with the previous studies of Altobelli *et al.* (1991). Since the inverse problem results in a discrete number of conductivities that are associated with the elements of the FE problem (conductivities are assumed constant in each element), the actual data take the form of discrete conductivity zones. An alternative method of presenting the data is in the form of contour plots. The contour plots are formed by associating the value of the conductivity within each element to the corresponding nodes. However, the boundaries of the elements contain three overlapping nodes. In these cases, simple averaging is used to determine the values on the boundaries. In this section, the data will be presented in one of two ways, either as a contour line plot or, if clearer, a colour contour plot.

6.1. *Negatively buoyant system*

The behaviour of the negatively buoyant system of heavy, conducting particles is discussed in this section. Contour plots are presented for concentration profiles at various stages towards the fully developed state. Additionally, the data are compared to the prediction of the model presented in § 4.

At a fully developed steady state, the concentration profile is expected to be symmetric about the vertical axis, and the experimental data confirms this assumption. Figure 9 presents the development of concentration profiles as the flow approaches the fully developed state for $N_b = 18.6$, the largest magnitude buoyancy number investigated. The potential measurements were obtained at four inline sensors placed at 5.5 m, 10.9 m, 12.4 m and 14.4 m after the inline mixer. This figure reveals an increase in particle deposition along the length of the flow system. By 5.5 m, there is already a significant accumulation of particles near the bottom of the pipe. Further down the pipe, at 10.9 m, a depletion zone near the top of the pipe is visible. The measurement furthest downstream (14.4 m) reveals a large deposition of particles at the bottom, a depletion zone at the top and nearly uniform distribution in the centre of the pipe. Although the pressure gradient did not seem to reach a constant value far downstream, the small differences between the particle concentration fields obtained

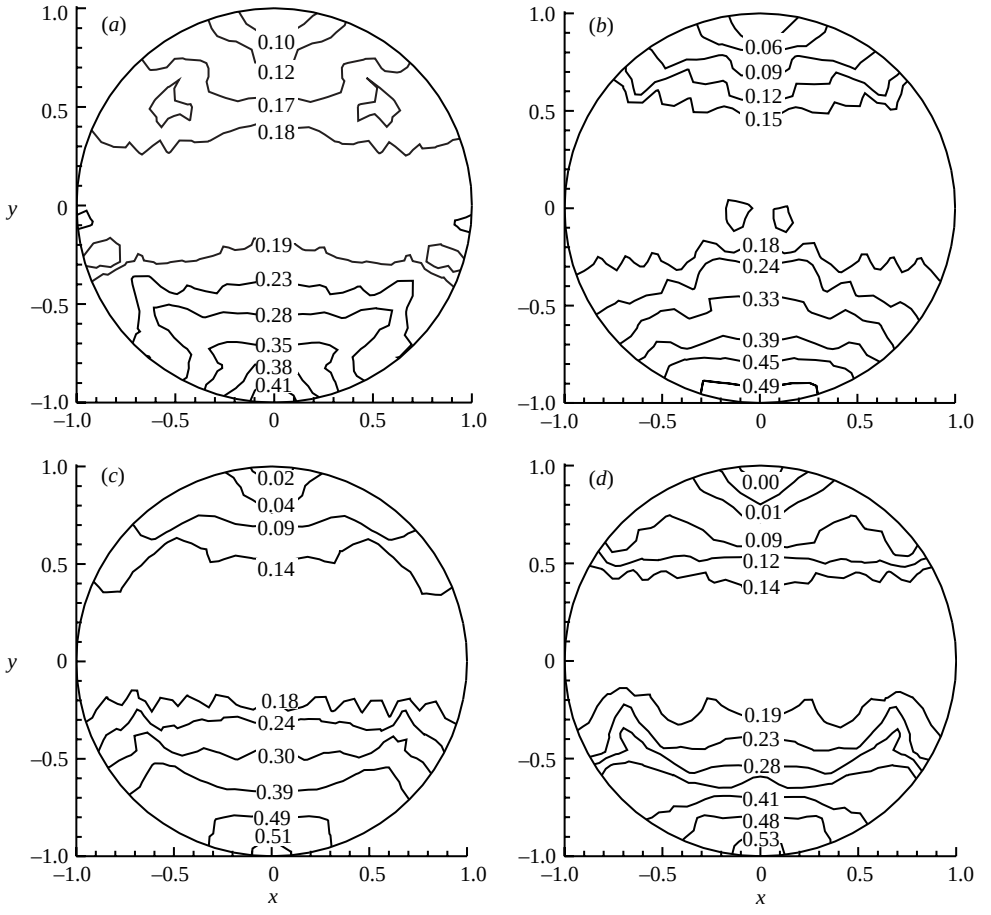

FIGURE 9. Contour plots of the concentration profile for a mixed suspension of bulk particle fraction, $\phi_b = 0.20$ and a buoyancy number, $N_b = 18.6$ at four locations downstream of the inline mixer. The average concentration, ϕ_{avg}, based on the integration of the contours is shown in parentheses. (*a*) 5.5 m (0.196); (*b*) 10.9 m (0.215); (*c*) 12.4 m (0.212); (*d*) 14.4 m (0.207).

at 12.4 m and 14.4 m indicate that the suspension flow is nearly fully developed. Further, it is important to note that the average concentrations determined from the profiles are well within 10% of the actual bulk fraction of 0.20.

Figure 10 presents the concentration profiles at 14.4 m downstream of the inline mixer for increasing buoyancy numbers. For the two larger values of N_b, there is little variation between the concentration profiles obtained at the two furthest downstream sensors, and hence it appears these suspension flows are nearly fully developed. However, this is not the case for the lowest buoyancy number in figure 10(*a*), and so this suspension may not be fully developed.

As the buoyancy number becomes larger, the deposition of particles becomes greater, or conversely as the buoyancy number becomes smaller, there is greater particle migration toward the central region of the pipe. As expected, there is a larger concentration of particles observed at the bottom of the pipe as the buoyancy number increases. The lowest buoyancy number reveals less deposition of the particles and a more uniform concentration of particles near the centre of the flow owing to shear-induced migration.

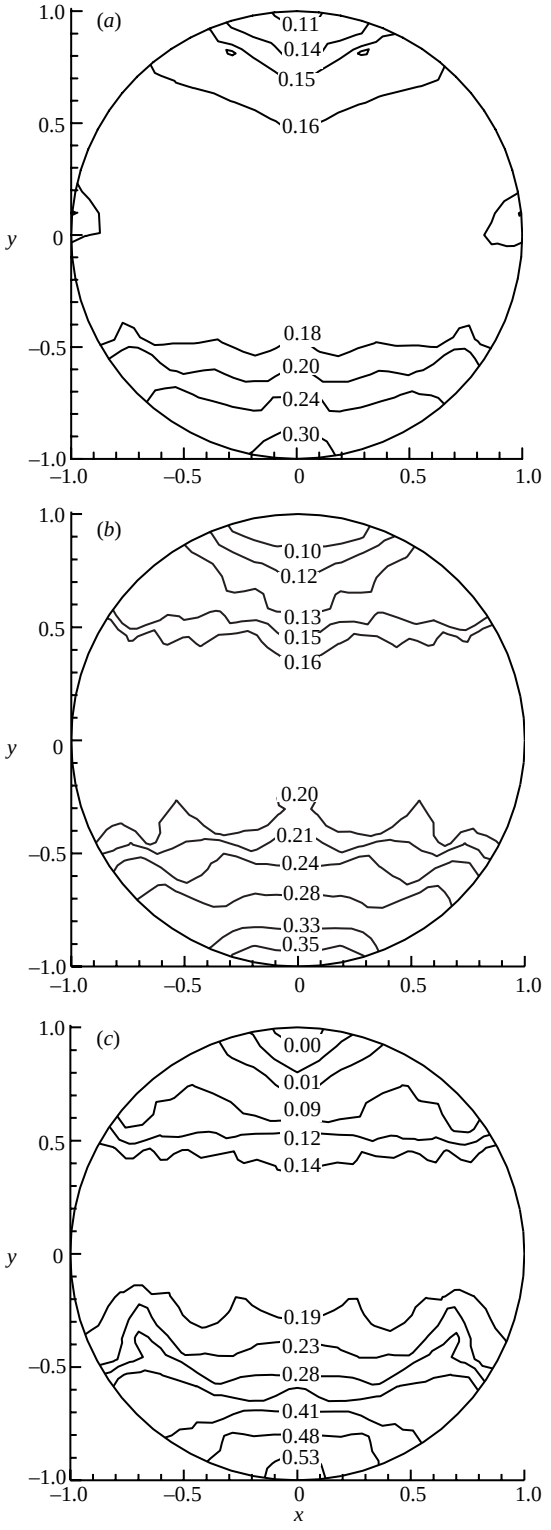

FIGURE 10. For caption see facing page.

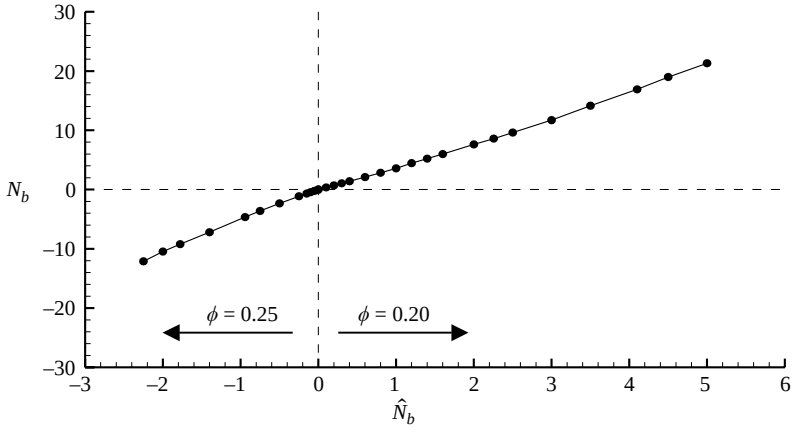

FIGURE 11. Theoretical correlation for the buoyancy number based on the average axial velocity, N_b, and the buoyancy number based on the pressure gradient, $\hat{N}_b$. The negative buoyancy numbers represent a suspension with a bulk volume fraction of 0.25 and the positive buoyancy numbers represent a suspension with a bulk volume fraction of 0.20.

One of the goals of this study was to determine if the suspension balance model qualitatively and quantitatively agreed with the concentration profiles obtained from EIT imaging. Therefore, the experimental results are compared with the predictions of the local isotropic version of the suspension balance model presented in §4. The natural buoyancy number for the numerical analysis is $\hat{N}_b = (\rho_p - \rho_g)g/G$ but $N_b = 2(\rho_p - \rho_f)gR^2/9\eta U$ is more easily calculated for the experiments using the average velocity. By requiring equivalent volumetric flow rates, the two buoyancy numbers are related as shown in figure 11. This figure was used to estimate $\hat{N}_b$ for the numerical simulations based on the experimental values of N_b.

Figure 12 represents the experimental volume fraction distributions compared to the prediction of the isotropic suspension balance model. All of the experimental data qualitatively match the prediction of this suspension model. Further, the suspension balance model and the experimental results predict similar particle concentrations at the depletion and accumulation zones at the top and bottom of the pipe, respectively. In addition, the theoretical and experimental images show similar curvatures in the concentration profiles. The largest variation in the experimental and theoretical data occurs at the centre of the pipe. The experimental data indicate a larger area of uniform particle distribution in the centre of the pipe, which varies minimally around the bulk concentration value. This portion of the imaging area is less sensitive to changes in conductivity (see Norman 2004), which may account for some of the uniformity of concentration found in the EIT images.

A significant difference in theoretical and experimental results is found at the lowest buoyancy number ($N_b = 4.9$). Although the experimental data and the numerical simulation predict reasonably similar results for the highest and lowest concentration, the theoretical result shows larger depletion and accumulation zones and more variation in the centre of the pipe, which may be partially attributed to the imaging

FIGURE 10. Contour plots of the concentration profile at 14.4 m downstream of the inline mixer for $\phi_b = 0.20$ and for all buoyancy numbers with the measured average concentration shown parenthetically. (*a*) $N_b = 4.9$ (0.208); (*b*) 9.5 (0.207); (*c*) 18.6 (0.207).

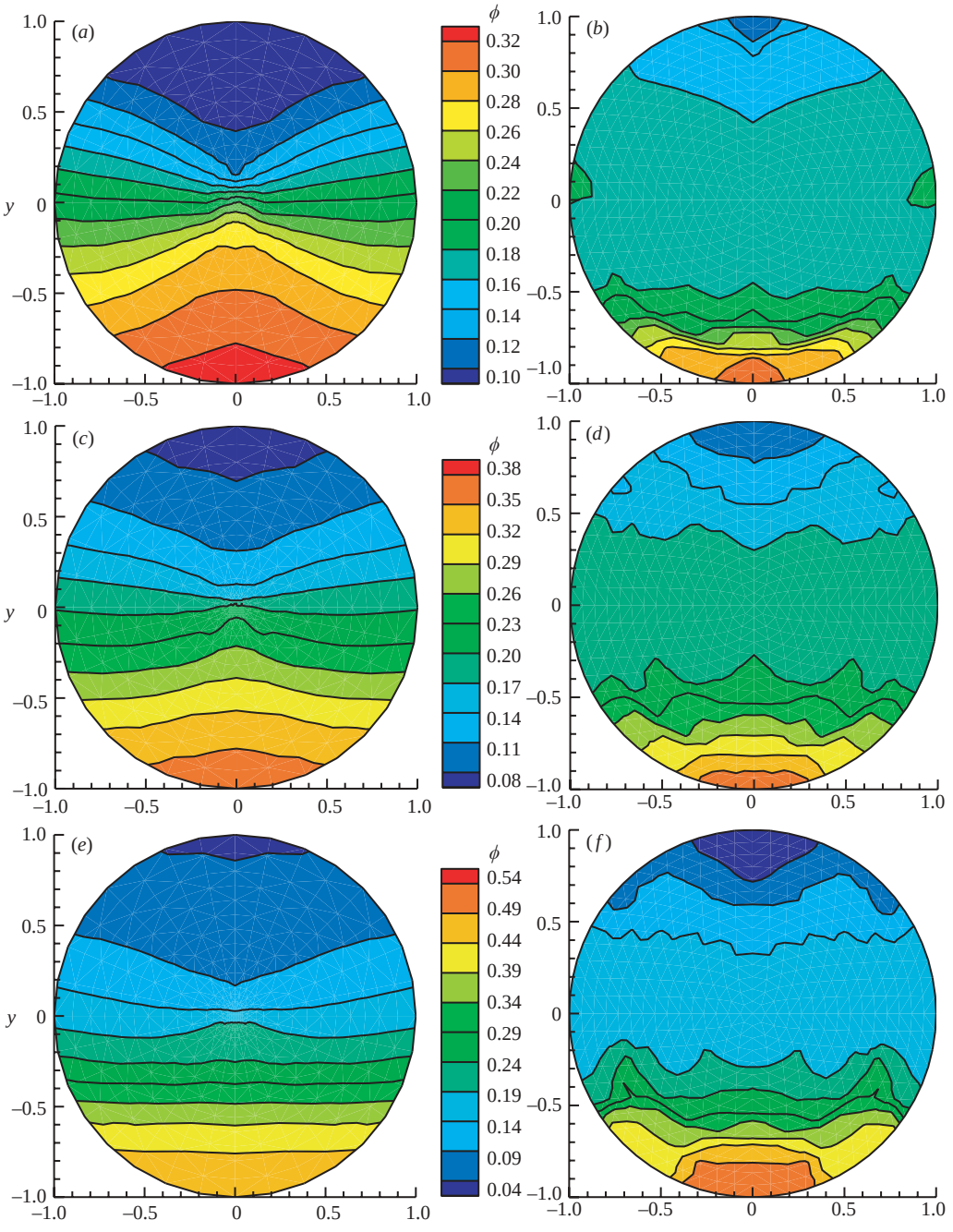

FIGURE 12. Comparison of theoretical (left-hand column) and experimental results (right-hand column) for the heavy particle suspensions. The experimentally obtained concentration profile are at 14.4 m downstream of the inline mixer for $\phi_b = 0.20$. The theoretical results were obtained using the local, isotropic suspension balance model. The data are presented for all experimental buoyancy numbers. (*a*) N_b4.9, theoretical; (*b*) 4.9, experimental; (*c*) 9.5, theoretical; (*d*) 9.5, experimental; (*e*) 18.6, theoretical; (*f*) 18.6, experimental.

technique. However, this concentration profile was obtained for a relatively large flow rate, hence a small buoyancy number, and most probably has not travelled a sufficient distance to achieve a fully developed flow (see § 7). Another significant discrepancy occurs between the theoretical and experimental concentration profiles for $N_b = 18.6$. Experimentally, there is a mounding of particles at the bottom of the pipe, contrary to the theoretical prediction of flat concentration profiles. Although there is only a small change in the concentration between 12.4 m and 14.4 m (figure 9), it may be that the highly viscous mound of particles is slow to relax to the flatter concentration profile predicted theoretically. This may explain the discrepancy between figures 12(*e*) and 12(*f*) and why the pressure gradient may not be fully developed at the end of the pipeline.

6.2. *Positively buoyant system*

This section discusses the results for the suspension flow of 25% by volume of light non-conducting particles (PMMA). The concentration profiles are presented as line contour plots or colour contour plots, and the results are compared to those predicted by the model presented in § 4.

Figure 13 presents the trends associated with increasing buoyancy number. Again, reduction of the flow rate controlled the magnitude of the buoyancy number and all the data were obtained from the sensor array at 9.8 m downstream of the inline mixer. Like the heavy particle suspensions, a larger concentration of particles accumulated at larger buoyancy numbers.

Again, one of the goals of this study was to compare the EIT images with the theoretical predictions of the suspension balance model. The model predictions qualitatively matched the experimental data, and these comparisons are presented in figure 14. As seen in the negatively buoyant suspensions, the experimental and theoretical results produce concentration values that are more closely matched at the top and bottom of the pipe. The largest variations in the experimental observations and theoretical predictions occur in the centre of the flow. These discrepancies may be attributed to the EIT imaging method, which is less sensitive to changes in the conductivity near the centre of the pipe and/or inadequacies in the theoretical model.

6.3. *Moment analysis*

To understand better the performance of the model as compared to the experimental observations, a moment analysis is used to compare the results quantitatively. Two moments, or integrals of the concentration fields, are defined to represent the vertical and horizontal distribution of particles at the fully developed axial length.

The first moment (M_y) represents the vertical distribution as given by

$$M_y \equiv \frac{1}{\phi_b} \int_A \phi(x, y) y \, \mathrm{d}A. \tag{6.1}$$

Here, ϕ_b is the bulk volume fraction, which is 0.25 for the light (PMMA) particle and 0.20 for the heavy (silver) particle suspension. Furthermore, the sign of this moment represents the relative buoyancy of the particles, where a negative sign indicates heavy particles and a positive sign indicates light particles.

The second moment (M_{x^2}) represents the horizontal distribution of the particles. This integral equation is given as

$$M_{x^2} \equiv \frac{1}{\phi_b} \int_A \phi(x, y) x^2 \, \mathrm{d}A, \tag{6.2}$$

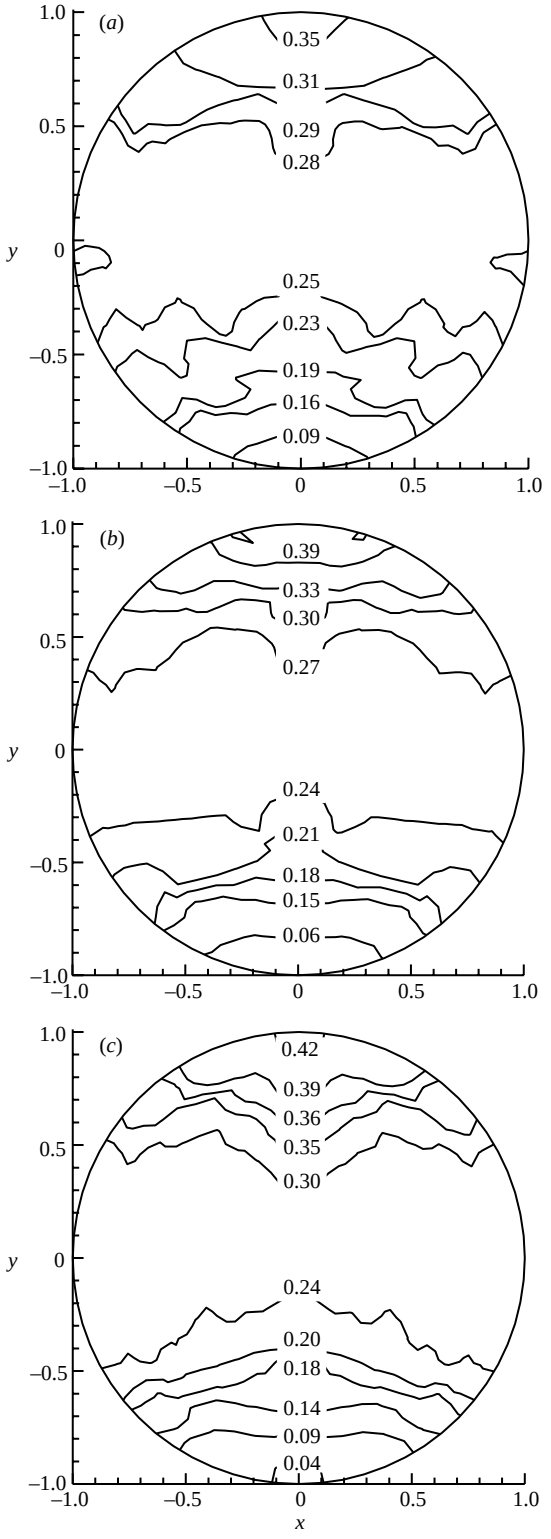

FIGURE 13. For caption see facing page.

where ϕ_b is the bulk volume fraction as defined for the first moment. This equation is a measure of the horizontal distribution around the centre of the pipe, where a small number indicates a large accumulation near $x = 0$ and increasing values indicate a spread of the particles on the horizontal axis.

Figure 15 show both moments for values of N_b (according to (1.1)) ranging from approximately -15 to 25, where the light particle suspension (negative N_b) represents an average volume fraction of 0.25 and the heavy (positive N_b) represent an average volume fraction of 0.20. There is reasonable agreement of the isotropic suspension balance model with the experimental results. As seen for the data for M_y, the suspension balance model and the experimental results display the same qualitative trend, indicating a similar distribution of the particles in the vertical direction. The theoretical and experimental agreement becomes more similar near the higher and lower magnitudes of buoyancy numbers. Additionally, this figure shows excellent quantitative agreement in the horizontal distribution of particles as indicated by M_{x^2}, though this moment is rather insensitive to N_b and ϕ. Overall, this figure indicates that the model matches fairly well the experimentally determined phase distribution of particles in a pressure-driven low-Reynolds-number suspension flow.

6.4. *Comparison to previous work*

It appears to date that the only previous published study on the pressure-driven flow of buoyant suspensions is that of Altobelli *et al.* (1991). They used NMRI to determine the velocity and concentration profiles of heavy particles in a viscous suspending fluid. However, most of their work was performed at small buoyancy numbers, and they were not able to resolve areas near the surface of the pipe. Their data are displayed for a buoyancy number of approximately 4.0 and a volume fraction of 0.23. Unfortunately, they only presented a qualitative scale for their results. Since they did not present a quantitative scale values were assigned to the qualitative scale using the reported value of maximum packing (0.58 ± 0.02) as a basis for the scale.

Figure 16(*a*) is the Altobelli *et al.* data using the assumptions described above. Figure 16(*b*) presents our experimental findings for a system of heavy conducting particles. The buoyancy number for our experiment was 4.9 with a bulk volume fraction of 0.20. Figure 16(*c*) represents the light non-conducting particles at a buoyancy number of -4.9 and a volume fraction of 0.25. This data was rotated 180°, for the purpose of comparison.

The first apparent difference in the NMRI studies and our experiments occurs at the boundary of the pipe. Altobelli *et al.* (1991) had difficulty resolving the concentrations at the boundary, which results in near maximum packing at these points (indicated by a white zone in figure 16*a*). They attributed this problem to either the resolution of the NMRI or the filtering algorithm they applied to the data. Regardless, similarities are apparent. First, all images resolve a depletion zone near the top, but their data reveal a much larger depletion zone with very little variation in the particle concentration compared to the study here. There is also a large zone in the centre of the pipe with concentrations between 0.16 and 0.24 for the NMRI data and both suspensions imaged in this study.

According to the dimensions (particle and pipe) reported by Altobelli *et al.*, the imaged suspensions should have travelled a sufficient distance to be a fully developed

---

FIGURE 13. Contour plots of the concentration profile at 9.8 m downstream of the inline mixer for $\phi_b = 0.25$ and for all buoyancy numbers with the measured average concentration shown parenthetically. (*a*) $N_b = -2.4$ (0.253); (*b*) -4.9 (0.250); (*c*) -10.1 (0.256).

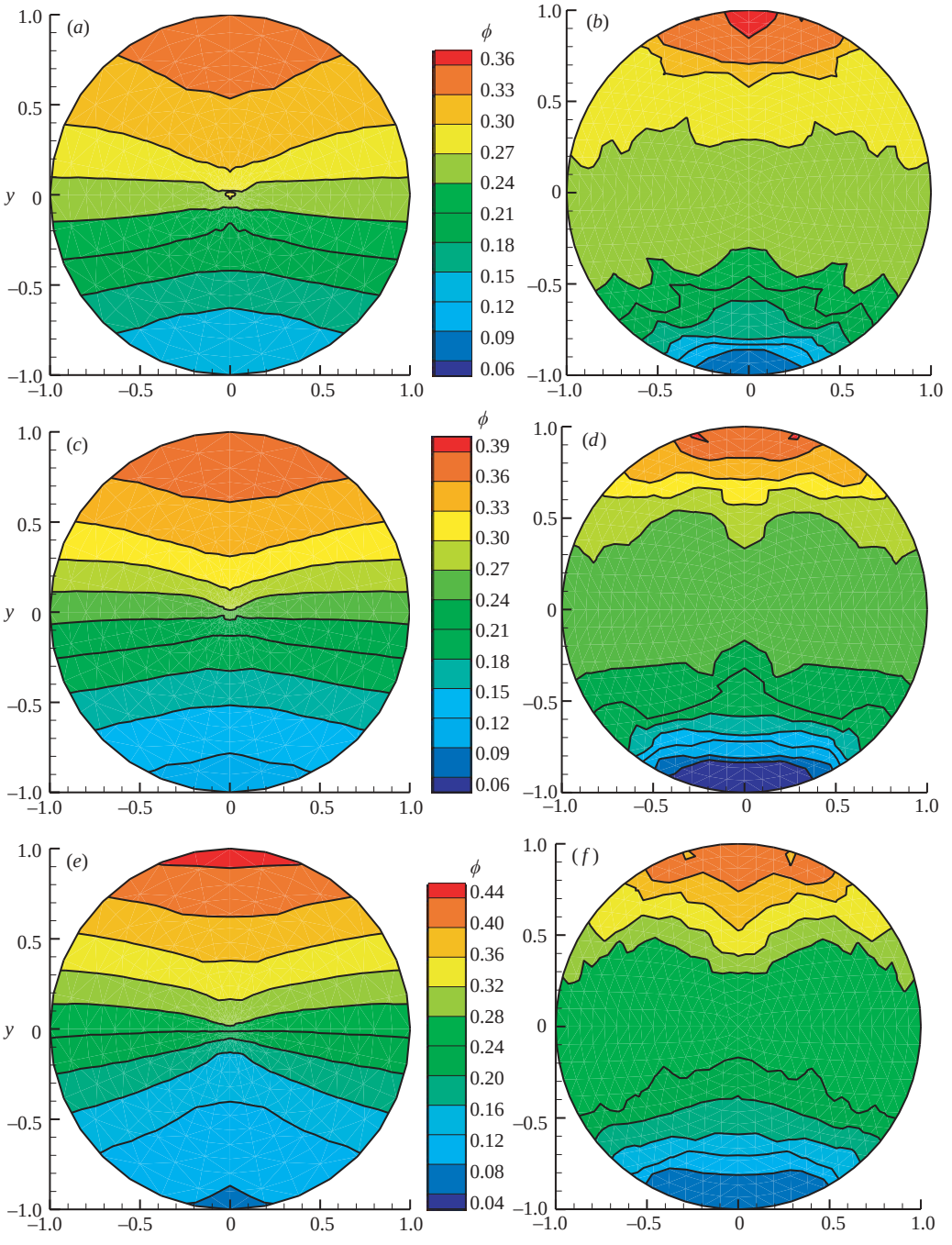

FIGURE 14. Comparison of theoretical (left-hand column) and experimental results (right-hand column) for the light particle suspensions. The experimentally obtained concentration profile are at 9.8 m downstream of the inline mixer for $\phi_b = 0.25$. The theoretical results were obtained using the local isotropic suspension balance model. The data are presented for all experimental buoyancy numbers. (*a*) $N_b = -2.4$, theoretical; (*b*) −2.4, experimental; (*c*) −4.9, theoretical; (*d*) −4.9, experimental; (*e*) −10.1, theoretical; (*f*) −10.1, experimental.

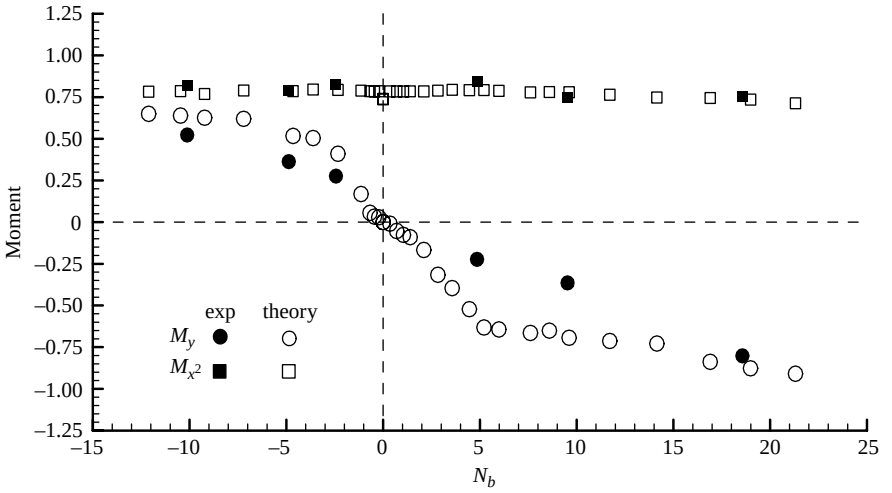

FIGURE 15. Moment comparison of the experimental results and the predictions of the isotropic suspension balance equations. The solid symbols represent the experimental results and the open symbols correspond to the suspension balance model. The circular symbols represent the moment M_y defined in equation (6.1) and the square symbols represent the moment M_{x^2} as defined in (6.2). Furthermore, the negative N_b values are normalized by a bulk fraction of 0.25 and the positive N_b values are normalized by a bulk volume fraction of 0.20, and these buoyancy numbers correspond to values shown in table 2.

flow (see § 7). While the concentration profile for the heavy particle suspension depicted in figure 16(*b*) may not be fully developed, the suspension of light particles in figure 16(*c*) appears to be fully developed. Therefore, the concentration profile from the light particle suspension in this study and the Altobelli *et al.* concentration field should be nearly identical (similar particle size and volume fraction of 0.23 for the Altobelli *et al.* study and 0.25 for the system investigated here). However, the EIT method resolved a high-concentration zone near the bottom of the pipe, which the Altobelli *et al.* method could not resolve, and the EIT images clearly reveal the trends expected for a buoyancy-dominated flow. Also, the curvature of the concentration field obtained from EIT imaging is similar to the predictions of the model, contrary to that of the NMRI.

7. Estimate of length to fully developed flow

One of the contributions of Nott & Brady (1994) was the scaling estimate of the length required to achieve a fully developed concentration profile for migration of neutrally buoyant particles; this parameter proved that earlier experimental results were not measured at sufficient lengths to ensure the flow was fully developed. However, the experimental studies presented here suggest that buoyant suspensions approach the fully developed state much earlier than predicted by Nott & Brady. This is not completely unexpected, because the scaling analysis of Nott & Brady was based on a diffusion mechanism. In buoyant systems, however, the important mechanism for determining the fully developed length scale is gravitational settling. Schaflinger, Acrivos & Stibi (1995) presented a scaling argument that considers gravitational settling in the prediction of the fully developed length scale. Here, a similar scaling argument is presented.

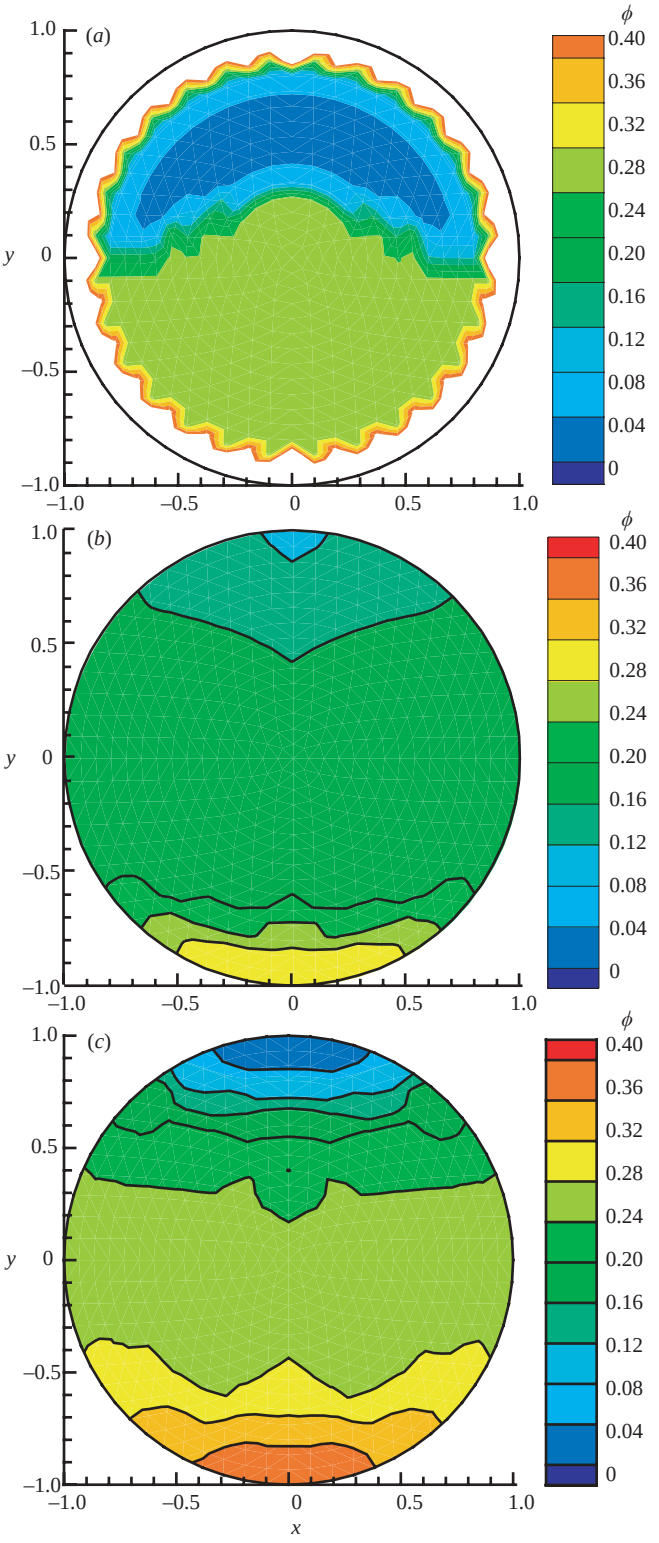

FIGURE 16. For caption see facing page.

By considering the time required for neutrally buoyant particles to migrate a distance of the order of the pipe radius and relating this steady-state time to the distance travelled for a mean flow velocity, the following expression was obtained by Nott & Brady (1994) for the length for fully developed flow in a pipe:

$$L_d \sim \frac{3}{32}\frac{R}{d(\phi)}\left(\frac{R}{a}\right)^2, \tag{7.1}$$

where $d(\phi)$ is a non-dimensional diffusion coefficient, R is the radius of the pipe, a is the radius of the particle and the subscript d indicates a diffusion dominated length scale.

As seen in these experiments, for systems dominated by buoyancy forces, (7.1) significantly overpredicts the fully developed length. For instance, the predicted length for fully developed flow for a suspension of the heavy particles used here is 1180 m (estimating the coefficients as $3/32d(\phi) \approx O(1)$); however, the experimental observations place this length closer to 14 m. Since this study focuses on buoyant systems in pipe flow, an alternative estimate of the fully developed length is presented here. Consider a pipe with a radius R. The time for the particles to traverse a distance of the order of the radius is given as

$$t_{ss} \sim \frac{R}{U_s f(\phi)}, \tag{7.2}$$

where, U_s is the Stokes settling velocity and $f(\phi)$ is the hindered settling function. The distance the particle travels horizontally can be related to the average suspension velocity by

$$L_b \sim U t_{ss}. \tag{7.3}$$

The subscript b denotes a buoyancy-dominated fully developed length and U is the average velocity of the suspension. Using this expression and the Stokes settling velocity results in the following estimate for the fully developed length:

$$L_b \sim \frac{9\eta R U}{2a^2(\rho_p - \rho_f)g}\frac{1}{f(\phi)}. \tag{7.4}$$

Using the definition of the buoyancy parameter in (1.1), the simplified estimate of the length for the fully developed flow of a buoyancy-dominated suspension is

$$L_b \sim \frac{R^3}{a^2 N_b}\frac{1}{f(\phi)}. \tag{7.5}$$

To emphasize the importance of using the correct scaling argument to determine the fully developed length, consider a viscous suspension flow in a pipe. The buoyancy dominated length scale is reduced by some fraction of N_b, so when N_b is greater than one (in many applications, N_b is often of the order of 10 or higher), the expression for the buoyancy-dominated fully developed length predicts significantly smaller lengths than predicted by the diffusion-dominated expression. For example, consider the heavy particle suspension at the largest buoyancy number presented in this study ($N_b = 18.6$).

FIGURE 16. (*a*) Particle concentration profiles measured by Altobelli *et al.* (1991) for a suspension of heavy particles with $\phi_b = 0.23$ and a buoyancy number of 4.0; (*b*) the concentration profile reported in this paper for the heavy particles with $\phi_b = 0.20$ and a buoyancy number of 4.9; (*c*) the concentration profile reported in this paper for the light particles with $\phi_b = 0.25$ and an experimental buoyancy number of -4.9.

The predicted length for a fully developed flow (L_d) is approximately 1200 m; however, the buoyancy-dominated length (L_b) is much shorter at approximately 159 m. Previous investigations have shown that the diffusion-dominated scaling predicts fully developed lengths longer than actually needed (Hampton *et al.* 1997). Butler *et al.* (1999) suggest that the actual value should be 0.12 L_d. Using this argument, the diffusion-dominated scaling predicts a length of 144 m, which is still much farther than observed experimentally. However, if the same coefficient is applied to the buoyancy-dominated expression, the predicted length is about 19 m, which is much closer to the experimentally observed value.

8. Conclusions

A non-invasive imaging technique was used here to study particle migration when buoyancy effects are important. The concentration profiles obtained using EIT reveal that buoyant suspension become fully developed earlier than neutrally buoyant systems, and a scaling argument similar to that introduced by Schaflinger *et al.* (1995) was presented as an estimate of the fully developed length of buoyant suspensions at low Reynolds numbers. Furthermore, it has been shown that the developing pressure gradient provides valuable insight into the progression towards the fully developed state. This study has shown that the pressure gradient drops initially and then increases to a larger fully developed value.

The experimental phase distributions were compared to the predictions of the model introduced by Nott & Brady (1994). This version of the suspension balance model produced results that qualitatively, and in some cases, quantitatively, matched the experimental data. The experimental results for the lowest-magnitude buoyancy number for the heavy particle suspensions did not match the predictions of the suspension balance model as closely; however, this is not completely unexpected, since some of the imaged suspensions may not have travelled a sufficient distance to become fully developed as described in § 7. Additionally, the theoretical predictions of the suspension balance model were compared with the experimental data using moments. This method revealed qualitative agreement of the theory with the experimental results.

In summary, EIT images have provided valuable insight into the behaviour of low-Reynolds-number suspension flows when buoyancy effects are important, and a comparison of these experimental observations with theoretical predictions has shown that the isotropic suspension balance model closely predicts the phase distribution qualitatively and in some cases quantitatively.

Appendix A. EIT forward modelling

The mathematical statement in (2.1) requires the solution of the forward problem (determination of the potentials at the electrodes, given a conductivity field). Ohm's law defines the forward problem in a low- frequency domain as

$$\nabla \cdot \sigma(\boldsymbol{x}) \nabla V = 0. \tag{A 1}$$

For this problem, the boundary conditions are defined as follows:

$$\boldsymbol{n} \cdot \sigma(\boldsymbol{x}) \nabla V = \begin{cases} q/A & \text{source electrode,} \\ -q/A & \text{sink electrode,} \\ 0 & \text{elsewhere,} \end{cases} \tag{A 2}$$

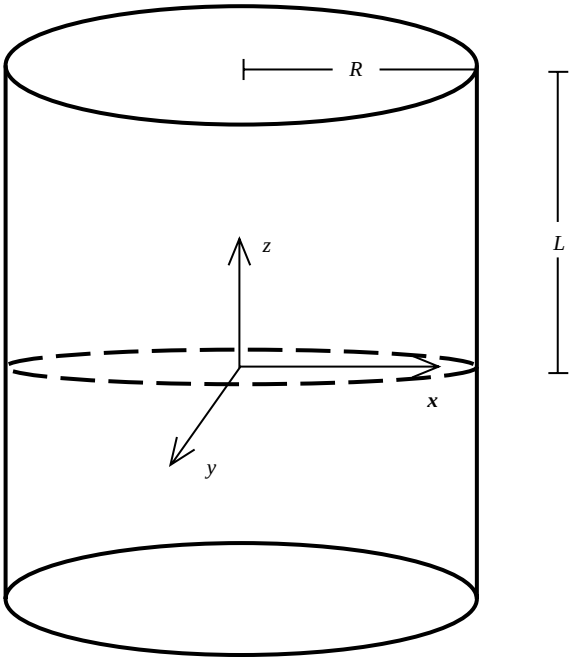

FIGURE 17. Cylindrical domain for Fourier expansion of the forward problem (pseudo-three-dimensional formulation).

where, $\boldsymbol{n}$ is the inward normal, V is the potential, q is the injection current and A is the area of the electrode. Ideally, the full three-dimensional problem would be solved; however, this problem is computationally expensive and the measurement technique used here does not produce enough data to perform a full three-dimensional analysis. Fortunately, the concentration profile of the suspension evolves slowly and so following Ider *et al.* (1990) the forward problem is assumed pseudo- three-dimensional by accounting for the axial invariance of the conductivity field. Consider the system shown in figure 17.

Following the methods of Ider *et al.*, the potential can be expanded in the Fourier series:

$$V(x, y, z) = \sum_{k=0}^{\infty} V_k(x, y) \cos\left(\frac{k\pi}{L} z\right), \tag{A 3}$$

where, k is the index and L is the length of propagation of the potential in the axial direction. Using this expansion and since the conductivity varies only in the cross-sectional plane, the following pseudo-three-dimensional expression for the forward problem is given by

$$\nabla_{2d} \cdot \sigma \nabla_{2d} V_k - \sigma \left(\frac{k\pi}{L}\right)^2 V_k = 0, \tag{A 4}$$

and the boundary condition is given in terms of the kth term in the cosine expansion:

$$\sigma \frac{\partial}{\partial \boldsymbol{n}} V_k = J_k, \tag{A 5}$$

where ∇_{2d} represents the two-dimensional gradient operator, J_k is the kth expansion of the current density (q/A) and $\boldsymbol{n}$ represents the inward normal. Clearly, these

expressions reveal that the solution of the forward problem is dependent on the number of expansions and the half-length of the cylindrical domain. In our experiments, the optimal half-length was determined as five times the radius of the pipe, and 11 ($k=0$ to 10) expansions were used.

Appendix B. EIT inverse modelling

The calculated potentials from (A 4) and (A 5) are used in the minimization problem given in (2.1). To find σ that minimizes the objective function, the derivative of (2.1) is set to zero. Expanding this derivative in a Taylor series yields the expression

$$\frac{\mathrm{d}(2\chi^2)}{\mathrm{d}\boldsymbol{\sigma}_{n+1}} = \frac{\mathrm{d}(2\chi^2)^T}{\mathrm{d}\boldsymbol{\sigma}_n} + \frac{(\boldsymbol{\sigma}_{n+1}-\boldsymbol{\sigma}_n)^T}{2}\cdot\frac{\mathrm{d}^2(2\chi^2)}{\mathrm{d}\boldsymbol{\sigma}_n{}^2} + O\left[(\boldsymbol{\sigma}_{n+1}-\boldsymbol{\sigma}_n)^2\right]. \tag{B 1}$$

The Taylor expansion is retained only up to $O(\boldsymbol{\sigma}_{n+1}-\boldsymbol{\sigma}_n)$, and the derivates in (B 1) are expanded in terms of (2.1) below:

$$\frac{\mathrm{d}(2\chi^2)}{\mathrm{d}\boldsymbol{\sigma}_n} = -\boldsymbol{J}_n^T\cdot\boldsymbol{W}_d^T\cdot\boldsymbol{W}_d\cdot(\boldsymbol{d}^{obs}-\boldsymbol{d}^{calc})_n + \lambda\boldsymbol{W}_m^T\cdot\boldsymbol{W}_m(\boldsymbol{\sigma}-\boldsymbol{\sigma}_r)_n, \tag{B 2}$$

$$\frac{\mathrm{d}^2(2\chi^2)}{\mathrm{d}\boldsymbol{\sigma}_n{}^2} = -\boldsymbol{G}^T\cdot\boldsymbol{W}_d^T\cdot\boldsymbol{W}_d\cdot(\boldsymbol{d}^{obs}-\boldsymbol{d}^{calc})_n + \boldsymbol{J}_n^T\cdot\boldsymbol{W}_d^T\cdot\boldsymbol{W}_d\cdot\boldsymbol{J}_n + \lambda\boldsymbol{W}_m^T\cdot\boldsymbol{W}_m.s \tag{B 3}$$

Equation (B 3) is the Hessian of the objective function given in (2.1). Further, the matrix $\boldsymbol{J}$ is the Jacobian, which is defined as

$$\boldsymbol{J} = \frac{\mathrm{d}}{\mathrm{d}\boldsymbol{\sigma}}(\boldsymbol{d}^{calc}). \tag{B 4}$$

The parameter $\boldsymbol{G}$ is the derivative of the Jacobian matrix, and is defined as

$$\boldsymbol{G} = \frac{\mathrm{d}^2}{\mathrm{d}\boldsymbol{\sigma}^2}(\boldsymbol{d}^{calc}). \tag{B 5}$$

The updated conductivity field using (B 1) and the above definitions is given by

$$(\boldsymbol{\sigma}_{n+1}-\boldsymbol{\sigma}_n) \cong \left[\boldsymbol{J}_n^T\cdot\boldsymbol{W}_d^T\cdot\boldsymbol{W}_d\cdot\boldsymbol{J}_n - \boldsymbol{G}_n^T\cdot\boldsymbol{W}_d^T\cdot\boldsymbol{W}_d\cdot(\boldsymbol{d}^{obs}-\boldsymbol{d}^{calc})_n + \lambda\boldsymbol{W}_m^T\cdot\boldsymbol{W}_m\right]^{-1}$$
$$\left[\boldsymbol{J}_n^T\cdot\boldsymbol{W}_d^T\cdot\boldsymbol{W}_d\cdot(\boldsymbol{d}^{obs}-\boldsymbol{d}^{calc})_n - \lambda\boldsymbol{W}_m^T\cdot\boldsymbol{W}_m\cdot(\boldsymbol{\sigma}-\boldsymbol{\sigma}_r)_n\right]. \tag{B 6}$$

The formation of the Jacobian and Hessian are computationally expensive, accounting for 75% or more of the inversion time. One option, which was used in this study, is to use a simplification such as a Gauss–Newton method (Torres-Verdín & Habashy 1993). This method ignores the second-order derivative in (B 3). Since the Jacobian results in the majority of the computational expense, the Jacobian was calculated using only the first expansion of the Fourier series ($k=0$), while the forward problem was expanded to the full $k=10$ expansions. When the error ceased to reduce, the inversion algorithm was implemented with the full expansion of the Jacobian ($k=10$). This reduced the computational time by approximately one-tenth of the full inversion scheme.

It is important to note that $\boldsymbol{W}_m$ can be chosen to specify many different constraints. For example, if $\boldsymbol{W}_m \equiv \boldsymbol{I}$, the solution will have the smallest deviation from the reference conductivity, and if $\boldsymbol{W}_m$ is chosen as the difference matrix (a representation of the first derivative), the solution will be the smoothest with respect to the reference conductivity (both of these criteria were used in this analysis). Furthermore, the regularization

parameter λ must be optimised within all iterations, which leads to a series of iterations within each conductivity update (in this analysis, λ is chosen as a fraction of the trace of the matrix $\boldsymbol{J}_n^T \cdot \boldsymbol{W}_d^T \cdot \boldsymbol{W}_d \cdot \boldsymbol{J}_n$ and is reduced, followed by a line search, until the smallest square error is found at that iteration).

Appendix C. Data processing

The potential measurements obtained from the Mk.2 data acquisition system are conditioned before any numerical processing is attempted. These conditioning factors are used to account for errors in the potential measurements resulting from geometric imperfections and electrode contact impedance. To determine the correction factors, a solution with the same conductivity of the suspending fluid is used to obtain potential measurements for each sensor array. The measured potentials are compared to the calculated potentials obtained from the forward problem (performed at the average current injection and same frequency as the experiments) discussed in Appendix A. These measurements are used to determine the conditioning factors, which are applied to all of the experimental data before any numerical processing is attempted. These correction factors are defined as follows:

$$\omega_i \left(\frac{V_c}{V_m} \right)_i , \tag{C 1}$$

where $(V_c)_i$ is the ith calculated potential from the forward algorithm, and $(V_m)_i$ is the ith potential measured with the Mk.2.

Each measurement is repeated several times, the results are averaged and the standard deviation is determined. If the potential varies more than one standard deviation then it is eliminated. Additionally, if a sign change occurs in any of the averaged data, that potential measurement is discarded. These two criteria are easily automated. Unfortunately, the Mk.2 potential measurements are very sensitive to small changes. If, for instance, a contaminant comes into contact with the electrode, an 'irregular' potential measurement may occur with minimal deviation in the averaged data. Determining these irregularities is difficult to automate and requires careful analysis of the data. Once an item of data is determined invalid using the above criteria, it must be eliminated. In general, the data-weighting matrix described in § 2 is a diagonal matrix consisting of the inverse of the square of the corresponding potential measurement. By simply changing the corresponding weight to a value of zero, the desired data points can be discarded.

Once the above conditioning is completed, the potential data was processed with the inverse algorithm. The corresponding suspending fluid conductivity was used as the initial guess. The inverse algorithm allows the reference conductivity to be either a single value applied to each component of the conductivity or individual values for each conductivity zone. This presents a method for incorporating *a priori* information into the inverse problem. Initially, the reference conductivity was set to a single value: the average of the initial guess (which for the first iteration is just the suspending fluid conductivity). The average reference value was updated at each iteration. Furthermore, the solution with the smallest deviation from the reference conductivity was enforced by setting $\boldsymbol{W}_m = \boldsymbol{I}$. The algorithm was stopped when either the error ceased to reduce or some predetermined limit was obtained (for instance, the error is usually limited to 0.10 to prevent noise from being inverted). Successive inversions were performed using the previous solution as a basis for the *a priori* information (the reference conductivity vector was assigned the values of the solution

from the previous inversion). Additionally, the model-weighting matrix was defined to determine the effects of changing from the smallest ($\boldsymbol{W}_m = \boldsymbol{I}$) and smoothest (difference matrix) regularization requirement. This procedure was continued until no significant change in the error was obtained or the error limit was reached. On average, this procedure resulted in a total of four inversions (limited to 20 iterations) for each set of potential measurements.

REFERENCES

Altobelli, S. A., Givler, R. C. & Fukushima, E. 1991 Velocity and concentration measurements of suspensions by nuclear magnetic resonance imaging. *J. Rheol.* **35**, 721–734.

Butler, J. E. & Bonnecaze, R. T. 1999 Imaging of particle shear migration with electrical impedance tomography. *Phys. Fluids* **11**, 1982–1994.

Butler, J. E., Majors, P. D. & Bonnecaze, R. T. 1999 Observations of shear-induced particle migration for oscillatory flow of a suspension within a tube. *Phys. Fluids* **11**, 2865–2877.

Carpen, I. C. & Brady, J. F. 2002 Gravitational instability in suspension flow. *J. Fluid Mech.* **472**, 201–210.

Cheney, M., Issacson, D. & Newell, J. C. 1999 Electrical impedance tomography. *SIAM Rev.* **41**, 85–101.

Dickin, F. & Wang, M. 1996 Electrical resistance tomography for process applications. *Meas. Sci. Technol.* **7**, 247–260.

Doyle, W. T. 1977 The Clausius–Mossotti problem for cubic arrays of spheres. *J. Appl. Phys.* **49**, 795–797.

Etuke, E. O. 1994 Impedance spectroscopy for component specificity in tomographic imaging. PhD thesis, University of Manchester Institute of Science and Technology.

Etuke, E. O., Bonnecaze, R. T. & Butler, J. E. 1999 Measurement and imaging of pulp consistency using electrical impedance tomography. *Proc. Tappi Conf. www.tappi.org*.

Fang, Z., Mammoli, A. A., Brady, J. F., Ingber, M. S., Mondy, L. A. & Graham, A. L. 2002 Flow-aligned tensor models for suspension flows. *Intl J. Multiphase Flow* **28**, 137–166.

Gadala-Maria, F. & Acrivos, A. 1980 Shear-induced structure in a concentrated suspension of solid spheres. *J. Rheol.* **24**, 799–814.

Hampton, R. E., Mammoli, A. A., Graham, A. L. & Tetlow, N. 1997 Migration of particles undergoing pressure-driven flow in a circular conduit. *J. Rheol.* **41**, 621–640.

Ider, Y. Z., Gencer, N. G., Atalar, E. & Tosun, H. 1990 Electrical impedance tomography of translationally uniform cylindrical objects with general cross-sectional boundaries. *IEEE Trans. Medical Imaging* **9**, 49–59.

Jenkins, J. T. & McTigue, D. F. 1990 Transport processed in concentrated suspensions: the role of particle fluctuations. *Two Phase Flows and Waves* **26**, 70–79.

Koh, C. J., Hookham, P. & Leal, L. G. 1994 An experimental investigation of concentrated suspension flows in a rectangular channel. *J. Fluid Mech.* **266**, 1–32.

Leighton, D. & Acrivos, A. 1987 The shear-induced migration of particles in concentrated suspension. *J. Fluid Mech.* **181**, 415–439.

Lyon, M. K. & Leal, L. G. 1998*a* An experimental study of the motion of concentrated suspensions in two-dimensional channel flow. Part 1. Monodisperse systems. *J. Fluid Mech.* **363**, 25–56.

Lyon, M. K. & Leal, L. G. 1998*b* An experimental study of the motion of concentrated suspensions in two-dimensional channel flow. Part 2. Bidisperse systems. *J. Fluid Mech.* **363**, 57–77.

Meredith, R. E. & Tobias, C. W. 1961 Conductivities in emulsions. *J. Electrochem. Soc.* **108**, 286–290.

Morris, J. F. & Boulay, F. 1999 Curvilinear flows of noncolloidal suspensions: the role of normal stresses. *J. Rheol.* **43**, 1213–1237.

Morris, J. F. & Brady, J. F. 1998 Pressure-driven flow of a suspension: buoyancy effects. *Intl J. Multiphase Flow* **24**, 105–130.

Nayak, H. V. 2001 Solutions of classes C^{00} and C^{11} for two dimensional Newtonian and viscoelastic fluid flows. PhD thesis, University of Kansas.

Nayak, H. V. & Carey, G. F. 2003 Least square finite element simulation of viscoelastic fluid flow through 4:1 contraction. *TICAM Rep. 03–24, ICES,* The University of Texas at Austin, Austin, Texas.

Norman, J. T. 2004 Imaging particle migration with electrical impedance tomography: an investigation into the behaviour and modelling of suspension flows. PhD thesis, The University of Texas at Austin, Austin Texas.

Nott, P. R. & Brady, J. F. 1994 Pressure-driven flow of suspensions: simulation and theory. *J. Fluid Mech.* **275**, 157–199.

Parker, L. R. 1994 *Geophysical Inverse Theory*. Princeton University Press.

Phillips, R. J., Armstrong, R. C., Brown, R. A., Graham, A. L. & Abbott, J. R. 1992 A constitutive equation for concentrated suspensions that accounts for shear-induced particle migration. *Phys. Fluids* A **4**, 30–40.

Schaflinger, U., Acrivos, A. & Stibi, H. 1995 An experimental study of viscous resuspension in a pressure-driven plane channel flow. *Intl J. Multiphase Flow* **21**, 693–704.

Shauly, A., Wachs, A. & Nir, A. 1998 Shear-induced particle migration in a polydisperse concentrated suspension. *J. Rheol.* **42**, 1329–1348.

Sierou, A. & Brady, J. F. 2002 Rheology and microstructure in concentrated noncolloidal suspensions. *J. Rheol.* **46**, 1031–1056.

Singh, A. & Nott, P. R. 2000 Normal stresses and microstructure in bounded sheared suspensions via Stokesian Dynamics simulations. *J. Fluid Mech.* **412**, 279–301.

Subia, S. R., Ingber, M. S., Mondy, L. A., Altobelli, S. A. & Graham, A. L. 1998 Modelling of concentrated suspensions using a continuum constitutive equation. *J. Fluid Mech.* **373**, 193–219.

Torres-Verdín, C. & Habashy, T. M. 1993 Cross-well electromagnetic tomography. 3*rd Intl Congr. Brazilian Geophys. Soc., Rio de Janeiro, Brazil* pp. 1–6.

Wallis, G. B. 1969 *One-dimensional Two-phase Flow*, p. 201. McGraw-Hill.

Zarraga, I. E., Hill, D. A. & Leighton, D. T. Jr 1999 The characterization of the total stress of concentrated suspensions of noncolloidal spheres in Newtonian fluids. *J. Rheol.* **44**, 185–220.

Zhang, K. & Acrivos, A. 1994 Viscous resuspension in fully developed laminar pipe flow. *Intl J. Multiphase Flow* **20**, 579–591.